




# Increasing the conductivity of V<sub>2</sub>O<sub>5</sub>-TeO<sub>2</sub> glass by crystallization: structure and charge transfer studies

Piotr Okoczuk<sup>1,\*</sup> , Natalia Anna Wójcik<sup>1</sup>, Leon Murawski<sup>1</sup>, Leszek Wicikowski<sup>1</sup>, Marcin Stanisław Łapiński<sup>1</sup>, Piotr Winiarz<sup>2</sup>, and Barbara Kościelska<sup>1</sup>

<sup>1</sup>Institute of Nanotechnology and Materials Engineering, Gdansk University of Technology, Narutowicza 11/12, 80-233 Gdańsk, Poland

<sup>2</sup>Department of Hydrogen Energy, Faculty of Energy and Fuels, AGH University of Science and Technology, al. Mickiewicza 30, 30-059 Kraków, Poland

Received: 1 December 2022

Accepted: 2 May 2023

Published online:  
21 May 2023

© The Author(s) 2023

## ABSTRACT

In the present paper, V<sub>2</sub>O<sub>5</sub>-TeO<sub>2</sub> glass was prepared by the melt-quenching technique. Crystallization of glass with a vanadium content higher than 35%mol results in an increase in electrical conductivity by a few orders of magnitude and a decrease in activation energy from ~0.40 to ~0.12 eV. In this work, a critical review of existing charge transfer models was presented on the example of V<sub>2</sub>O<sub>5</sub>-TeO<sub>2</sub> glass and glass-ceramics. Schnakenberg's and Friedman-Triberis' charge transfer models were found to be applicable to both glass and glass-ceramics. Optical phonon frequencies obtained from Schnakenberg's model are in agreement with FTIR studies. Values of activation energies obtained from the Schnakenberg model decrease after crystallization. Friedman-Triberis' model shows an increase in the density of states near the Fermi level from 10<sup>19</sup> - eV<sup>-1</sup> cm<sup>-3</sup> in glass, to 10<sup>21</sup> eV<sup>-1</sup> cm<sup>-3</sup> in glass ceramics. Structural studies show that the main crystallizing phase is Te<sub>2</sub>V<sub>2</sub>O<sub>9</sub> which occurs with the V<sub>2</sub>O<sub>5</sub> shell in glasses with compositions 50–50%mol and 45–55%mol. It is concluded that crystallization results in the reduction of vanadium ions in the remaining glass matrix which leads to an increase in the V<sup>4+</sup>/V<sup>5+</sup> ratio and therefore, an increase in electrical conductivity.

## Introduction

Electrical conductivity in glasses containing transition metal oxide (TMO) was intensively studied by many researchers because of their interesting

conductive and optical properties and potential applications as cathode and anode materials, switches, and others [1–8]. However, that cannot be said about the partially crystallized TMO glass-ceramics. It was noticed that partially crystallized samples containing V<sub>2</sub>O<sub>5</sub> exhibit conductivity higher

Handling Editor: Andrea de Camargo.

Address correspondence to E-mail: piotr.okoczuk@pg.edu.pl

by a few orders of magnitude [2]. In the past years, Pietrzak and Garbarczyk et. al. [9–12] were investigating the structural origin of the conductivity enhancement in the crystallized vanadate systems but no DC conductivity investigation was performed in the TMO glass–ceramics yet. In the  $P_2O_5$ - $V_2O_5$  it was recognized that crystallization of the glass results in the presence of the core–shell structures, in which highly disordered  $V_2O_5$  constitutes the shell of the crystallites [13]. The crystallization under DC monitoring and isothermal differential scanning calorimetry (DSC) investigation showed that the structure of conductive elements in the crystallized  $P_2O_5$ - $V_2O_5$  glass–ceramics is two-dimensional [13].

The conduction mechanism was well described in binary and ternary TMO glasses in terms of hopping of the small polaron (SPH) [2, 3]. It was recognized that in most TMO glasses electron mobility is very low because of its interaction with the lattice of the material, whether it is crystalline or vitreous [14]. An excess electron located near a group of atoms distorts the lattice, resulting in the appearance of a potential well in which electrons become localized. That state of the electron is called polaron, in which the radius ( $r_p$ ) corresponds to the size of lattice distortion caused by the trapped electron. The depth of the potential well is called polaron binding energy ( $W_H$ ). To move the electron to another position an external field has to supply the energy equal to polaron binding energy plus, in disordered systems, a part of distortion energy ( $W_D$ ). Because of the strong interaction with the lattice, electron hopping is strongly associated with lattice distortions caused by optical and acoustic phonons. The contribution of the mentioned phonons changes with the temperature and one can distinguish three regions: ( $T > \theta_D/2$ ), ( $\theta_D/2 > T > \theta_D/4$ ), and ( $T < \theta_D/4$ ), where  $\theta_D$  is the Debye temperature. In the high-temperature region ( $T > \theta_D/2$ ), mainly optical phonons contribute to the conductivity, at low temperatures ( $T < \theta_D/4$ ), optical phonons are frozen out, and acoustic phonons play a dominant role in the conduction process. At the intermediate range of temperatures ( $\theta_D/2 > T > \theta_D/4$ ) both, optical and acoustic phonons are considered in the SPH. Due to differences in the interaction of the glass network with the environment depending on the temperature, different conductivity models are used in different temperature ranges: Mott SPH in high and low temperatures (Eqs. 4,6)[15], Schnakenberg SPH in intermediate

temperatures (Eqs. 8, 9)[16]. However, as phonon frequencies of acoustic and optical phonons differ, an additional Debye-like temperature parameter referring to optical phonons was introduced  $-\theta_{OP}$ , which was the theme of discussion in the 90' [10–12]. According to Bridge and Higazy [17], Debye temperature for acoustic phonons ( $\theta_{AC}$ ) is two times lower than obtained from calculations for optical phonons ( $\theta_{OP}$ ) (from conductivity and IR absorption studies) in the CoO- $Co_2O_3$ - $P_2O_5$  system. El-Mallowany [18, 19] in his studies shows, that in the tellurite glasses, the ratio between  $\theta_{AC}$  and  $\theta_{OP}$  is around 3.5–3.6. To separate respecting temperature ranges for fitting of charge transfer models, Debye temperature of  $V_2O_5$ - $TeO_2$  glass in a DC investigation has often been taken as one relating to acoustic phonons ( $\theta_D$ ), the value of which is around  $\theta_{AC} = 240K$  [20]. Optical Debye temperature from infra-red studies  $\theta_{OP}(IR)$  in vanadate glasses was reported to be around  $\theta_{OP}(IR) = 1000 - 1200K$  [21–23], but no optical Debye temperature from DC conductivity investigation  $\theta_{OP}(el)$  has been determined yet in the  $V_2O_5$ - $TeO_2$  glass or glass–ceramics. As in the Schnakenberg model only  $W_H$  is a temperature-dependent parameter (its changes depend only on the decay of optical phonons), separation of temperature ranges for accurate charge transfer models fitting should be in respect to  $\theta_{OP}$ . If one assumes  $\theta_{OP} = 1000 - 1200K$ , then the multi-phonon temperature range should be considered in the temperature range of ( $\theta_{OP}/2$ ) = 600 – 500K to ( $\theta_{OP}/4$ ) = 300 – 250K.

In very low temperatures ( $T < \theta_D/4$ ), Mott proposes that the preferable way of electron transfer may be due to variable range hopping (VRH). Greaves [5] has extended that theory by multi-phonon influence on electron transport. The latter two models refer to the linear behavior of the conductivity versus  $T^{-1/4}$  which is found to be applicable to most TMO glass [4, 5]. The same dependency of conductivity was predicted by Friedman and Triberis [24] in the percolation approach of SPH.

This paper shows the method of determining the crystallization parameters of vanadium oxide-containing glass to achieve the maximum conductivity of the glass–ceramics. Optical phonon frequencies in the  $V_2O_5$ - $TeO_2$  vitreous and partially crystallized system from the FTIR studies and the fitting of the Schnakenberg model of SPH were examined for the first

time. Detailed analysis of DC conductivity in  $V_2O_5$ - $TeO_2$  glass and partially crystallized  $V_2O_5$ - $TeO_2$  glass-ceramics was performed with the most popular charge transfer models for TMO glass. As clustering of vanadium and tellurium oxides during crystallization is highly possible and was considered by previous researchers in amorphous materials [2], we will also examine Shimakawa's multi-phonon hopping model for  $V_2O_5$ - $TeO_2$  glass and glass-ceramics. A novel method of analysis of activation energy temperature dependence in a wide range of temperatures was presented. With analysis of obtained results, suitable charge transfer in  $V_2O_5$ - $TeO_2$  glass-ceramics was established and associated with observed structural changes caused by crystallization. In this paper, the first detailed analysis of vanadium-tellurite glass-ceramics was presented.

## Experimental

Glass samples were prepared using reagent grade  $V_2O_5$  (Acros Organics, 99.6 + %) and  $TeO_2$  (Acros Organics, 99 + %). Powders in molar proportions from 30 mol%  $V_2O_5$ -70 mol%  $TeO_2$  to 50 mol%  $V_2O_5$ -50 mol%  $TeO_2$  with a 5% step (later called "30V/70T" for 30% mol  $V_2O_5$ -70% mol  $TeO_2$ , "35V/65T" for 35% mol  $V_2O_5$ -65% mol  $TeO_2$  etc.) were mixed in the agate mortar. Batches of 10 g of mixed powders were melted in the furnace in the silica crucibles (covered with a silica plate) at a temperature of 1073 K for 30 min. The melt was poured on the cold steel plate and pressed with another steel plate resulting in samples within ~1 mm thick. Obtained glass samples were annealed at 383 K for 10 h.

The DSC measurements were performed using the NETZSCH DSC 204 F1 Phoenix in a synthetic air atmosphere with a heating rate of 5 K  $min^{-1}$  in the covered aluminum crucible using the average mass of the sample of 2 mg. The maximum temperature of measurement was 673 K for samples 50V/50T and 45V/55T, and 723 K for samples 40V/60T, 35V/65T, and 30V/70T. The Proteus 7 software was used for the determination of glass transition ( $T_g$ ) temperatures, the onset of crystallization peaks ( $T_{conset}$ ), and a maximum of crystallization peaks ( $T_{cx}$ ) where  $x$  is the number of a peak.

To obtain the time of annealing, after which samples exhibit the maximum possible conductivity

value, the DC conductivity of samples was studied in isothermal conditions of annealing, selected from DSC thermograms. The crystallization temperature was selected to avoid deformation of the sample and to obtain the crystallization time that would allow it to be carried out with the available equipment. For the isothermal annealing upon in-situ DC monitoring, samples were polished with sandpaper to the thickness  $l \sim 0.6$  mm for obtaining a smooth sample surface. For the measurement, gold electrodes with a diameter of ~0.9 cm were evaporated on the surface of the samples. To establish the electrical contact between the sample and the sample holder, platinum wire and silver paste were used. The resistance of the samples was measured by a 2-wire method with the usage of a Keysight 34907 A multimeter with data acquisition. The authors used the 2-point method due to the relatively high resistance of the material (much higher than the resistance of measurement leads, contacts, and electrochemical reactions on the electrodes). To calculate the conductivity of the sample, the dependence  $\sigma = l/(R * A)$  (where  $\sigma$  is the conductivity of the sample,  $R$  is the measured resistance, and  $A$  is the area of the electrode) was used. The crystallization with in-situ monitoring of changes in electrical conductivity was performed in the furnace built of a special ceramic heater controlled by a dedicated PXR4 Fuji temperature controller, with a temperature precision of ~0.1 °C. After establishing the parameters of annealing, the external crystallization was performed using the Carbolite EHA 12/150B to prepare samples for later studies. The crystallization with in-situ monitoring of changes in electrical conductivity and external crystallization were performed using the same K-type thermocouple mounted in the furnace. Crystallizations were performed in the air atmosphere.

Partially crystallized samples that were obtained after the isothermal crystallization applied to measure in-situ changes in electrical conductivity will be addressed as "50V/50T cr.", "45V/55T cr.", etc. Some of the samples underwent crystallization for 24 h at the temperature of crystallization peak from DSC thermograms (602 K for 50V/50T and 679 K for 30V/70T) for better determination of crystalline phases developing during crystallization (later called "fully crystallized"). Fully crystallized samples were used only for XRD analysis.

The structure of as-quenched and heat-treated samples was examined by XRD using an X'Pert Phillips diffractometer with Cu K $\alpha$  radiation (1.541 Å). The XRD measurements were carried out on the powdered samples at room temperature. The diffraction patterns of crystallized samples were analyzed using the HighScorePlus software package [25].

FTIR analysis in the IR region of 4000–400 cm<sup>-1</sup> was carried out using the PerkinElmer Frontier spectrometer in the transmission mode using dried KBr as a medium. A mixture of the powdered sample and KBr in a proportion of 1/50 was pressed with the force of 2 tons for 2 min to form a tablet. The measurement was averaged from 16 scans with a resolution of 4 cm<sup>-1</sup>.

The topography of samples was observed by using an Olympus LEXT OLS4000 Confocal Scanning Laser Microscope (CSLM). The maximum magnification of the used lens was 100x, with an optical magnification of 2160x. CSLM measurements were obtained from the fresh intersection of the sample.

The x-ray photoelectron spectroscopy (XPS) measurement was performed using an Argus (Omicron NanoTechnology, Taunusstein, Germany) x-ray photoelectron spectrometer. The photoelectrons were excited by an Mg–K x-ray source. The x-ray anode was operated at 15 keV and 300 W. The XPS measurement was performed at room temperature under ultra-high vacuum conditions, with pressures below  $1.1 \times 10^{-8}$  mbar. For self-consistency, the C1s line of 285 eV binding Energy was used as a reference for all charge shift corrections as this peak arises from hydrocarbon contamination and it's generally accepted as a remaining constant. Samples had to be studied without argon sputtering to avoid the reduction of vanadium and tellurium in the sample. Data analysis was performed with the CASA XPS software package (Casa Software Ltd., ver. 2.3.23., Devon, UK), using a Shirley background subtraction and the least-square Gaussian–Lorentzian curve-fitting algorithm.

For the AC conductivity measurements, gold electrodes were evaporated at the polished surface of the glass and glass–ceramics samples. Impedance measurements were carried out in the frequency range from 10 mHz to 1 MHz with an AC voltage of 1 V<sub>rms</sub> at the temperature range from 153 to 413 K with the Novocontrol Concept 40 broadband dielectric

spectrometer. The measurements were done under a nitrogen atmosphere with a temperature step of 10 K. An additional AC conductivity study at temperatures up to  $T_g$  point was made using Novotherm HT 1600 Controller with a step of 5 K in an air atmosphere to investigate the activation energy of the conduction mechanism at high temperatures. The maximum temperature of measurement depended on the  $T_g$  point of the studied sample. All electrical measurements and the results of fitting are affected by a measurement error not exceeding 2%.

The density of the samples was measured according to the Archimedes principle, using water as an immersion liquid. Measurements were conducted at room temperature and repeated 3 times to minimize the error. The average value was taken as the result. The average distance  $R$  between vanadium ions was calculated from the dependence  $R = N^{-1/3}$  [26], where  $N$  is the concentration of vanadium ions per unit volume, which was estimated from the composition of glass and measured density.

## Results and discussion

### Crystallization of glass

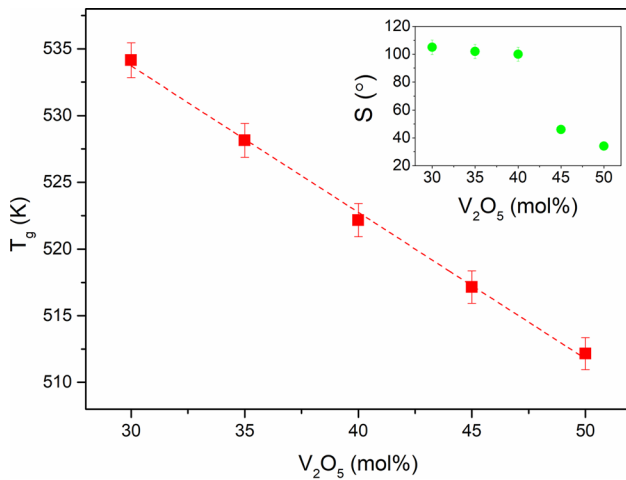
All DSC thermograms of prepared glass show distinctive glass transition points visible as endothermic drift, and exothermic processes correlated with crystallization.  $T_g$ ,  $T_{conset}$ ,  $T_{cx}$ , and glass stability ( $S$ ) were determined and shown in Table 1. Samples with composition from 30V/70T to 40V/60T show only one crystallization peak at temperatures around 673 K. Samples with compositions 45V/55T and 50V/50T show also multiple crystallization peaks between 548 and 653 K (Fig. 2d). Values of  $T_g$  for all glass samples are listed in Table 1 and presented in Fig. 1 as a function of V<sub>2</sub>O<sub>5</sub>. It can be seen that  $T_g$  decreases with vanadium content linearly, from 512 K for the 50V/50T sample to 534 K for the 30V/70T sample.  $S$  (calculated using  $S = T_g - T_{conset}$ ) show a sudden decrease for glasses 45V/55T and 50V/50T.

The next step was the controlled crystallization of glass. Results of isothermal annealing upon DC conductivity monitoring for samples 50V/50T, 45V/55T, and 40V/60T are presented in Fig. 2. Samples 35V/65T and 30V/70T showed no changes in electrical



**Table 1** Temperatures obtained from DSC measurements

Sample	$T_g$ (°K)	$T_{\text{conset}}$ (°K)	$T_{c1}$ (°K)	$T_{c2}$ (°K)	$T_{c3}$ (°K)	S (°)
50V/50T	512	546	576	602	610	34
45V/55T	517	563	575	603	620	46
40V/60T	522	622	676	–	–	100
35V/65T	528	630	670	–	–	102
30V/70T	534	639	679	–	–	105

**Figure 1**  $T_g$  dependence on vanadium oxide content. The inset shows the glass's thermal stability behavior.

conductivity; therefore they were not investigated further in terms of electrical transport studies.

Temperatures of crystallization presented in Fig. 2a–c with respect to DSC thermograms are shown in Fig. 2d. To obtain the maximum conductivity value possible, the annealing time was determined as 32 h and 20 min for the 50V/50T sample, 439 h for the 45V/55T sample, and 115 h for the 40V/60T sample. The annealing of sample 50V/50T was much quicker than this observed in the 45V/55T sample despite a higher temperature of annealing and a smaller gap to the first crystallization peak. It can be seen that the conductivity of all samples increased by about one order of magnitude. Moreover, despite the lack of a crystallization peak in the DSC curve, the conductivity increase in sample 40V/60T is equal to the samples with higher vanadium content.

### Topography and structure of as-quenched and heat-treated samples

The amorphous structure of as-quenched samples was confirmed by the X-ray diffraction method and

the results are shown in Fig. 3. No reflections can be observed except for a characteristic bump around 20–35° typical for glasses. In Fig. 4 exemplary x-ray patterns of crystallized samples 50V/50T, 40V/60T, and 30V/70T are shown. Diffractograms of 50V/50T cr. sample, which exhibited maximum conductivity, and a fully crystallized 50V/50T sample are shown in Fig. 4a. As can be seen in Fig. 4a a fully crystallized sample is composed of two phases:  $\text{Te}_2\text{V}_2\text{O}_9$  ( $2\text{TeO}_2 \cdot \text{V}_2\text{O}_5$ ) (dominating) and  $\text{V}_2\text{O}_5$  (second phase). An XRD diffractogram of the 50V/50T cr. sample shows only a few broad maximums indicating the beginning of crystallization. Similar results were obtained for the 45V/55T cr. sample. A fully crystallized 30V/70T sample (Fig. 4b) shows that in the low vanadium content glasses (below 33 mol%  $\text{V}_2\text{O}_5$ ), the second phase is  $\text{TeO}_2$ . No second phase was observed in the 40V/60T and 35V/65T samples.

The molar ratio of tellurium in 50V/50T, 45V/55T, and 40V/60T samples is significantly lower in the glass matrix than in the  $\text{Te}_2\text{V}_2\text{O}_9$  crystallites. With the growth of the  $\text{Te}_2\text{V}_2\text{O}_9$  ( $2\text{TeO}_2 \cdot \text{V}_2\text{O}_5$ ) phase, the surrounding of the crystallite is depleted of tellurium leaving a vanadium-rich area near the crystallites. As a formation of  $\text{Te}_2\text{V}_2\text{O}_9$  crystallites with an oxygen content lower than that of the as-quenched glass matrix may result in an oxygen-rich region around the  $\text{Te}_2\text{V}_2\text{O}_9$  crystallites, the vanadium-enriched area is believed to be in the form of  $\text{V}_2\text{O}_5$  crystals (in samples 50V/50T cr. and 45V/55T cr.).  $\text{V}_2\text{O}_5$  crystallites may also nucleate separately.

Using the XRD data, crystalline phase contribution in samples after the annealing was calculated using the formula:  $K = 100\% * I_p / (I_p + I_A)$ , where  $K$  is the % of crystalline phase present in the samples,  $I_p$  is an area under the peaks of the crystalline phase, and  $I_A$  is an area under the amorphous halo. Crystallinity for samples 50V/50T cr., 45V/55T cr., and 40V/60T cr. equals, respectively: 3%, 3%, and 20%.

The effect of the crystallization process on the morphology of as-quenched and heat-treated

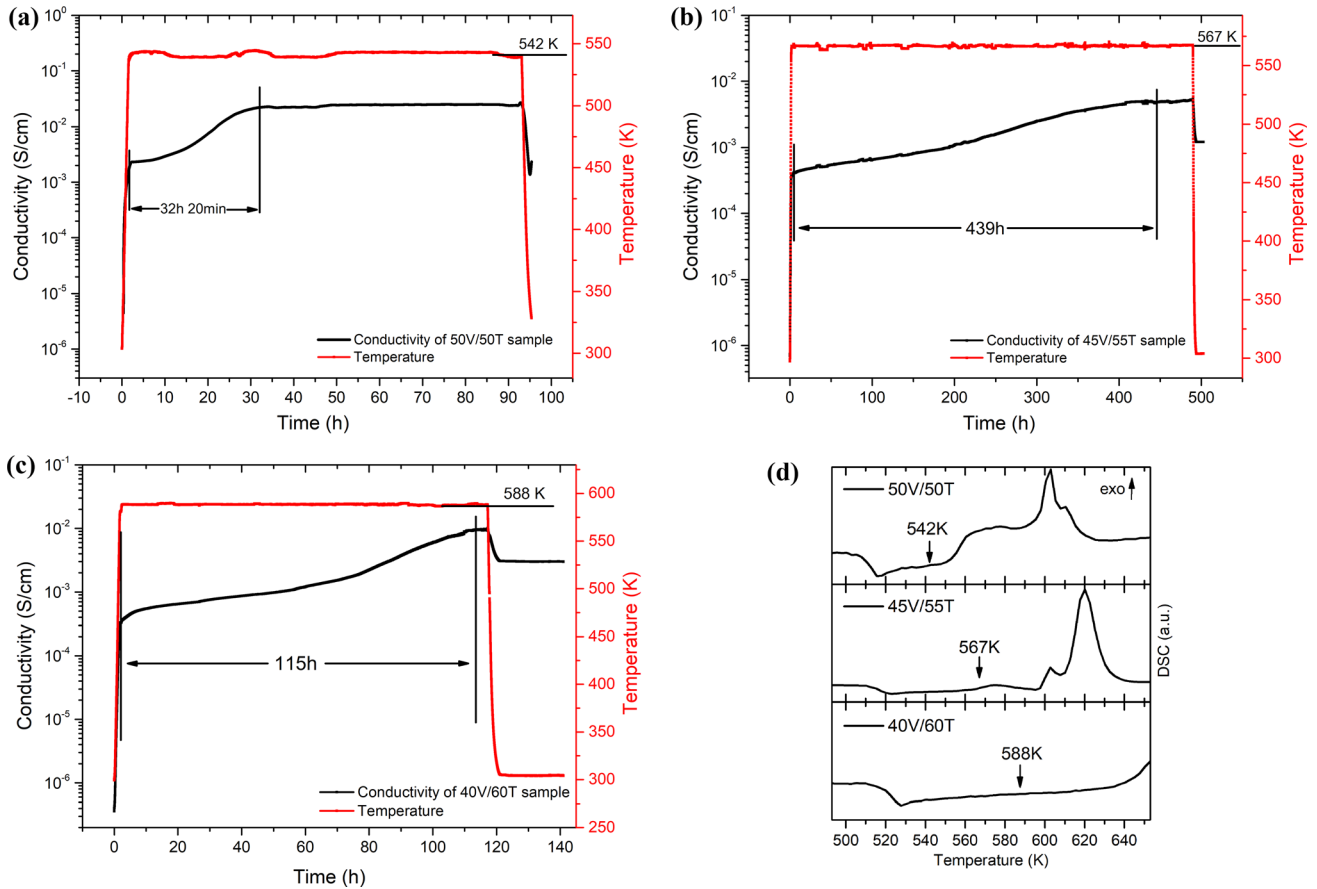


**Figure 2** Time dependence of conductivity and temperature during annealing of the sample: **a** 50V/50T, **b** 45V/55T, and **c** 40V/60T, with **d** DSC curves with crystallization temperatures marked.

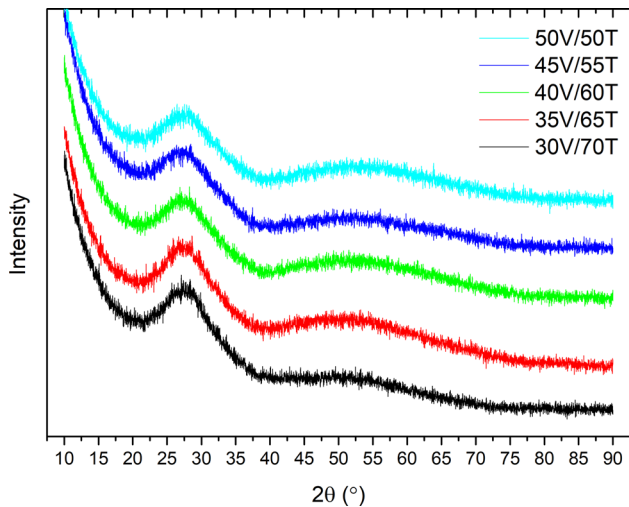


**Figure 3** X-ray diffractograms of glass.

samples was investigated. In Fig. 5 confocal microscopy images of samples cross-sections are shown. Figure 5a presents the topography of an exemplary 50V/50T sample. The other glasses exhibit

homogenous topography with no visible structures, similar to sample 50V/50T. Annealed samples show two phases of different refractive indexes, which, based on the XRD results, can be interpreted as agglomerates of crystallites dispersed in the glass matrix. Size of crystallites present in the 50V/50T cr. sample (Fig. 5b) is in the range of < 1–20 μm. In the 45V/55T cr. sample (Fig. 5c), crystallites seem to be smaller, in the range of < 1–10 μm. No specific shape of crystallites can be observed. Both 50V/50T cr. and 45V/55T cr. samples look similar. The image of the crystallized 40V/60T sample (Fig. 5d) shows large crystallites in the shape of needles, where crystallization proceeds from the surface.

The effect of crystallization on the glass structure and the optical frequencies interacting with the material were also studied by FTIR. All glass spectra are shown in Fig. 6. To determine the position and contribution of the bands to the spectrum, deconvolution was performed. Each peak's meaning is described below. The band present at around

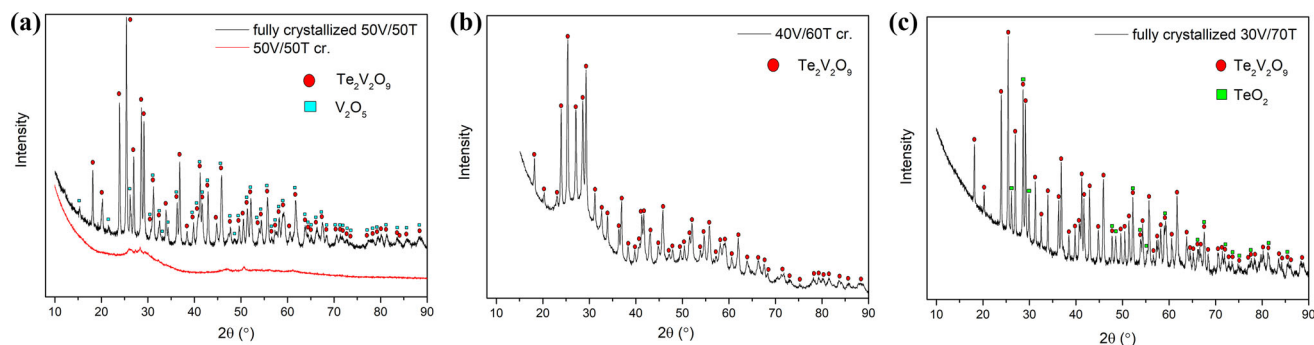


**Figure 4** X-ray diffractograms of annealed samples: **a** 50V/50T, **b** 40V/60T, and **c** 30V/70T.

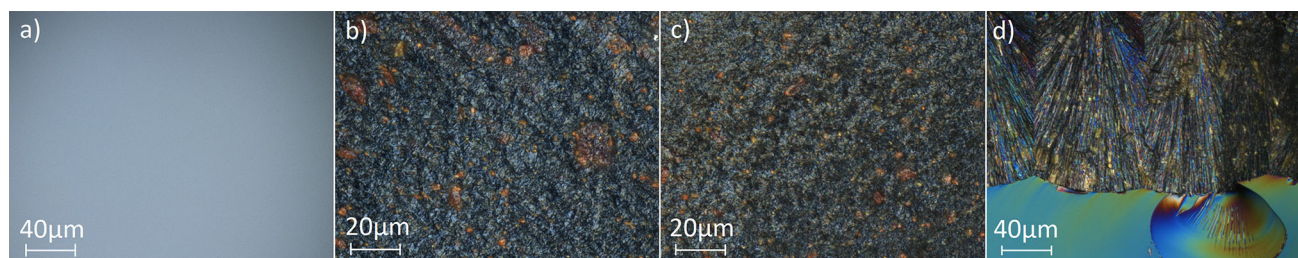


**Figure 5** Confocal images of **a** 50V/50T, **b** 50V/50T cr, **c** 45V/55T cr, **d** 40V/60T cr.

$1020\text{ cm}^{-1}$  (1st band,) is assigned to the V=O bond of non-degenerated  $\text{VO}_5$  groups (as in crystalline structures). It can be seen that the 1st band, responsible for the non-degenerated V=O bond, fades out with lower content of vanadium in samples. The more structure of  $\text{VO}_5$  deviates from the ideal, the V=O band shifts to lower wavenumbers. In the imperfect structure of  $\text{V}_2\text{O}_5$ , the V=O bond exists at around  $1000\text{ cm}^{-1}$  (2nd band)(degenerated  $\text{VO}_5$  groups), in our case at  $1005\text{ cm}^{-1}$  [23, 27, 28]. The more Te ions are added, the more V=O bonds are replaced with weaker degenerated V=O bonds, V–O–V and V–O–Te bonds, in sample 50V/50T 2nd band and 4th band is most likely overlapped by a band of  $980\text{--}970\text{ cm}^{-1}$  of the free  $\text{VO}_2$  groups of the  $\text{VO}_4$  polyhedrons (3rd band), which is visible in sample 30V/70T at  $980\text{ cm}^{-1}$ . V–O–V bond can be also recognized by bands around  $960\text{--}910\text{ cm}^{-1}$  (4th band),  $920\text{--}915\text{ cm}^{-1}$  (5th band), and  $> 800\text{ cm}^{-1}$  (6th band) responsible for, respectively: symmetric stretching of  $\text{VO}_2$  groups, anti-symmetric stretching of  $\text{VO}_2$  groups, and V–O–V bridges [23, 27]. It is known that  $\text{TeO}_4$  groups are transforming into  $\text{TeO}_3$  groups under the influence of the addition of  $\text{V}_2\text{O}_5$ . The band around  $790\text{--}770\text{ cm}^{-1}$  (7th band) can be described as a sign of symmetric vibrations of  $\text{TeO}_3$  groups or a V–

O–V bond in the  $\text{V}_2\text{O}_5$  structure as well as in the  $\text{VO}_2$  structure [29–31].  $\text{TeO}_3$  groups can also be recognized by the band around  $665\text{--}680\text{ cm}^{-1}$  (8th band) while the  $\text{TeO}_2$  group band is present at around  $635\text{--}610\text{ cm}^{-1}$  (9th band) [27, 32]. Upshifting of the 8th band in the vanadium-rich samples is a sign of a higher polymerization degree of the  $\text{TeO}_2$  network or an intensity increase in the  $\text{VO}_2$  groups' broad band present also at around  $715\text{ cm}^{-1}$  [30]. A band at  $500\text{ cm}^{-1}$  (10th band) is due to symmetric linkage vibrations in  $\text{TeO}_4$  polyhedra [29] or V–O–V octahedral bending modes in  $\text{VO}_2$  [30].

Comparing the FTIR spectra of glasses it is found that the various content of  $\text{V}_2\text{O}_5$  influences the intensity of the band at  $500\text{ cm}^{-1}$ . One would also notice that depending on the content of  $\text{V}_2\text{O}_5$ , the high-frequency limit of the glass is shifting from around  $1050\text{ cm}^{-1}$  in the 30V/70T sample to  $1183\text{ cm}^{-1}$  in the 50V/50T sample.

Figure 7 shows a comparison of the as-quenched and annealed samples 50V/50T, 45V/55T, and 40V/60T. In both 50V/50T cr. and 45V/55T cr. annealed samples, a sharp shoulder-like band exists at  $1020\text{ cm}^{-1}$ , which is a characteristic band of  $\text{V}_2\text{O}_5$  in a crystalline form. That band is not present in sample 40V/60T cr. All annealed samples show a decrease in

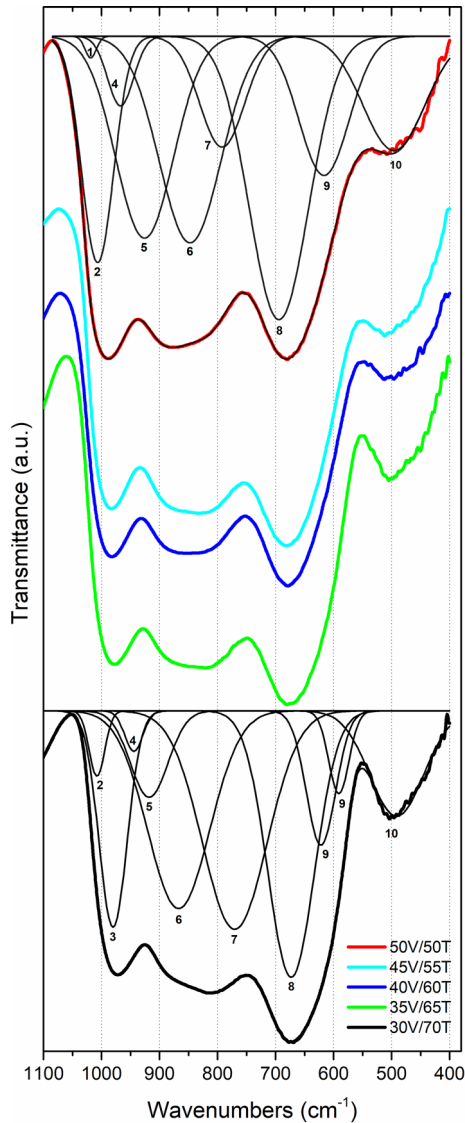
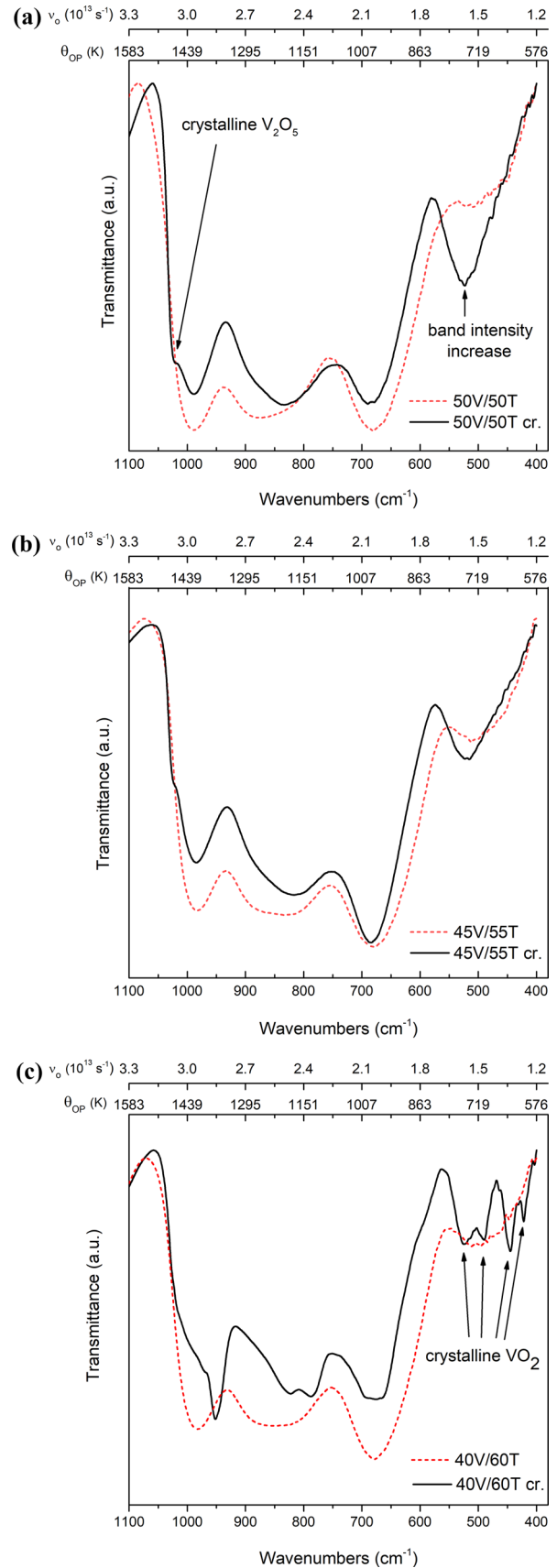


**Figure 6** FTIR spectra of all glass samples with a deconvolution of 50V/50T and 30V/70T samples spectra.

the intensity of the band at  $880\text{ cm}^{-1}$ , which can be interpreted as the partial loss of the degenerated  $\text{VO}_5$  groups, which segregate into non-degenerated  $\text{VO}_5$  groups. Significant changes of the  $500\text{ cm}^{-1}$  band in the annealed samples show that vanadium oxide organizes into  $\text{VO}_2$  groups. In the 40V/60T cr. sample, the formation of  $\text{VO}_2$  groups can be confirmed by the presence of these bands at a position typical for  $\text{VO}_2$  crystallites [30].

**Figure 7** Comparison of **a** 50V/50T, **b** 45V/55T, and **c** 40V/60T samples before and after crystallization.





The infra-red studies of tellurite glasses have been conducted by El-Mallawany [18, 19] to determine the optical Debye temperature, which denotes the average optical frequency in tellurite glasses. In the polaron model of hopping conduction in vitreous materials, the Debye optical parameter can be written as:

$$\theta_{OP} = \frac{hv_o}{k}, \quad (1)$$

where  $v_o$  denotes the optical frequency in the material. Additional axes are added in Fig. 7 to visualize the range of the  $\theta_{OP}(IR)$  and the optical phonon frequency  $v_o$ .

As shown previously in the glass, changes in the position of the band lead to a decrease in average  $\theta_{OP}(IR)$  with a decrease in vanadium content. A decrease in average  $\theta_{OP}(IR)$  can also be seen after crystallization, as the intensity of the bands around  $500\text{ cm}^{-1}$  increases, and a decrease in the high-frequency limit can be noticed.

Preliminary XPS studies of 50V/50T and 50V/50T cr. samples show, that upon crystallization  $V2p_{3/2}$  peak changes its position by 0.2 eV toward lower binding energy (Fig. 8a) which can be a sign of a small increase in the  $V^{4+}/V^{tot}$  ratio.  $Te\ 3d_{5/2}$  peak preserves its position after crystallization (Fig. 8b). Deconvolution confirms the small increase of  $V^{4+}$  valence state of vanadium in the annealed sample (Fig. 8c). The difference in ratio between  $Te^{4+}$  and  $Te^{6+}$  remains the same before and after crystallization (Fig. 8d).

As can be seen in Figs. 1, 4b, and 5d, despite conductivity enhancement, crystallization of the sample 40V/60T occurs differently than in glass with higher vanadium content. XRD, along with DSC (Fig. 4, Table 1) shows that the only crystallizing phase in the sample 40V/60T is the  $Te_2V_2O_9$  ( $2TeO_2 \cdot V_2O_5$ ), which crystallizes in the shape of needles. In samples 50V/50T, and 45V/55T most probably it is the vanadium-rich shell of  $Te_2V_2O_9$  crystals that stops the growth of the  $Te_2V_2O_9$  in a shape similar to that observed in 40V/60T cr. (Fig. 5d). FTIR spectroscopy of sample 40V/60T cr. (Fig. 7c) shows characteristic bands of the  $VO_2$  around  $500\text{ cm}^{-1}$  whose crystallites cannot be observed on the XRD plot. A similar enhancement of the intensity of the bands around  $500\text{ cm}^{-1}$  can be noticed in the FTIR spectra of samples 50V/50T cr. and 45V/55T cr. (Fig. 7a, b). During the crystallization of the  $Te_2V_2O_9$  ( $2TeO_2 \cdot V_2O_5$ )

phase in the 50V/50T and 45V/55T samples, excess vanadium left in the glass matrix after crystallization of  $Te_2V_2O_9$  oxidizes to form a crystalline  $V_2O_5$  shell around  $Te_2V_2O_9$  crystallites. The oxygen content in  $V_2O_5$  is higher than in the as-quenched glass and the  $Te_2V_2O_9$ , therefore it should be expected that oxygen migration to the  $V_2O_5$  crystallites takes place. Both of the crystalline phases contain vanadium in the oxidation state of (5+). These premises lead us to the conclusion that during crystallization, vanadium in the remaining glass matrix is reduced by the creation of a  $V_2O_5$  shell in a manner shown in Fig. 9; therefore, the ratio of  $V^{4+}/V^{5+}$  is increased in the glassy part of the glass-ceramics, which is supported by preliminary XPS studies (Fig. 8) (samples 50V/50T cr., 45V/55T cr., 40V/60T cr.). A glass with similar or lower vanadium content than the  $Te_2V_2O_9$  crystal does not show a change in the electrical conductivity upon crystallization because the majority of vanadium is contained in the  $Te_2V_2O_9$  crystals.

## Electrical properties

### Small polaron hopping

The AC conductivity dependence on the frequency in amorphous materials usually obeys the Jonsher law in the form of [33]:

$$\sigma'(\omega) = \sigma_{DC} + Af^{s(T)} \quad (2)$$

where  $\sigma_{DC}$  is the DC conductivity and  $\sigma_{AC} = Af^{s(T)}$  is the AC component. The DC conductivity region dominates in the low-frequency region and the AC component in the high-frequency region. All of the glass samples fulfill the Jonsher law. The fitting of Eq. (2) is performed to obtain  $\sigma_{DC}$  and the  $s$  components. Example results of the fitting are shown in Fig. 10 for sample 50V/50T. The obtained  $\sigma_{DC}$  values will be considered in a further investigation (Fig. 11c, d). The AC study of the sample 40V/60T cr. was not possible due to the significant deformation of the sample caused by the annealing process.

In general, the electrical conductivity of semiconductors is well described by the Arrhenius-type equation:

$$\sigma = \sigma_0 \exp\left(-\frac{W}{kT}\right), \quad (3)$$

Where,  $\sigma_0$  is a pre-exponential factor,  $W$  is the activation energy,  $k$  is the Boltzmann constant and  $T$  is

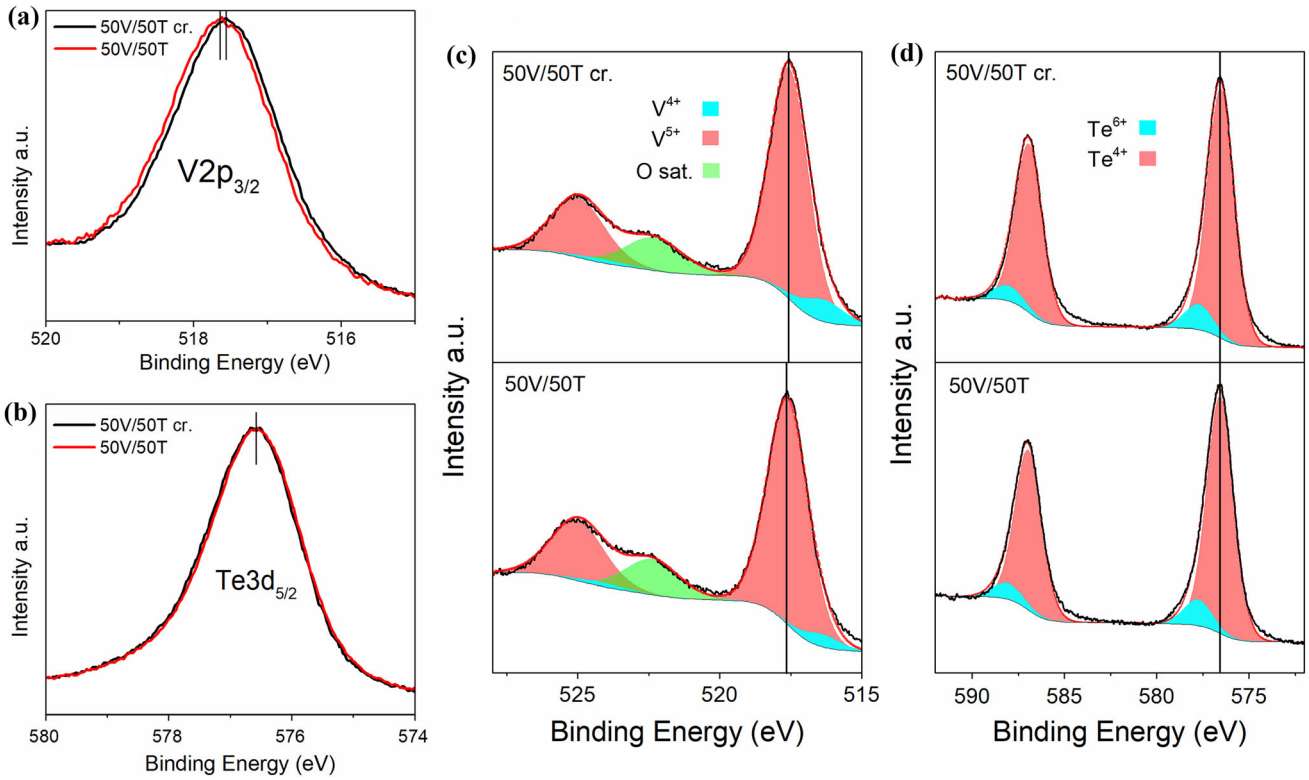


**Figure 8** Comparison of **a** V2p<sub>3/2</sub> and **b** Te3d<sub>5/2</sub> position in 50V/50T and 50V/50T cr. samples. Deconvolution of **c** V 2p and **d** Te 3d spectra in 50V/50T and 50V/50T cr. samples.

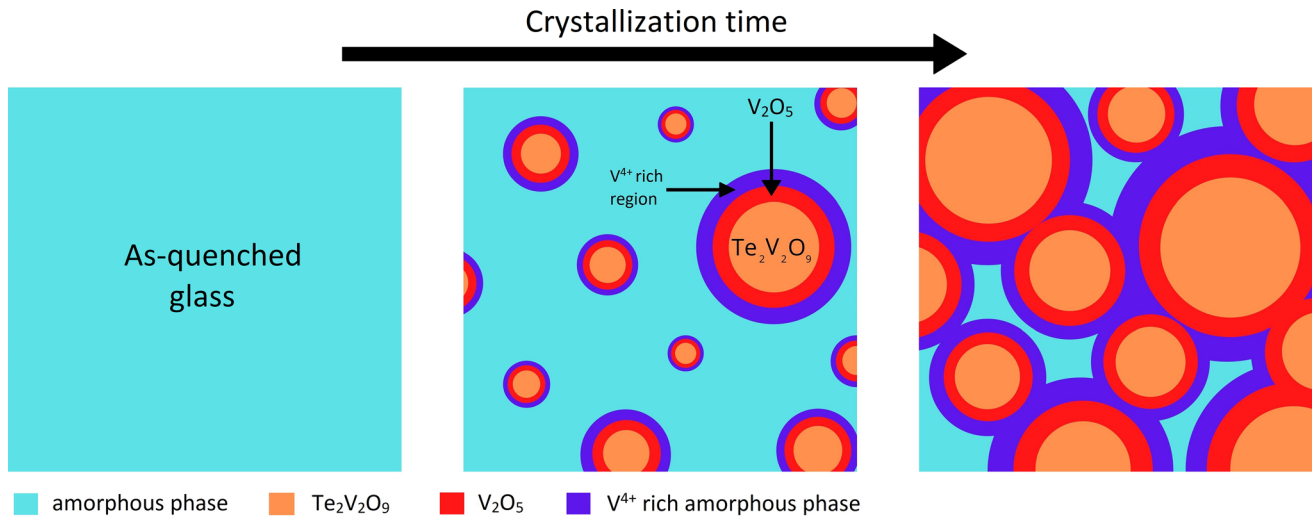


**Figure 9** Scheme of the crystallization mechanism in samples 50V/50T and 45V/55T.

the absolute temperature. Conductivity temperature dependence of the small polaron movement at high- and low-temperature regions was well described by Austin and Mott [34]. In their approach, activation energy obeys the dependency of [34, 35]:

$$W = W_H + \frac{1}{2} W_D \text{ for } T > \theta_D/2 \quad (4)$$

$$W = W_D \text{ for } T < \theta_D/4$$

For the intermediate range of temperatures ( $\theta_D/2 > T > \theta_D/4$ ), Mott proposes Schnakenberg

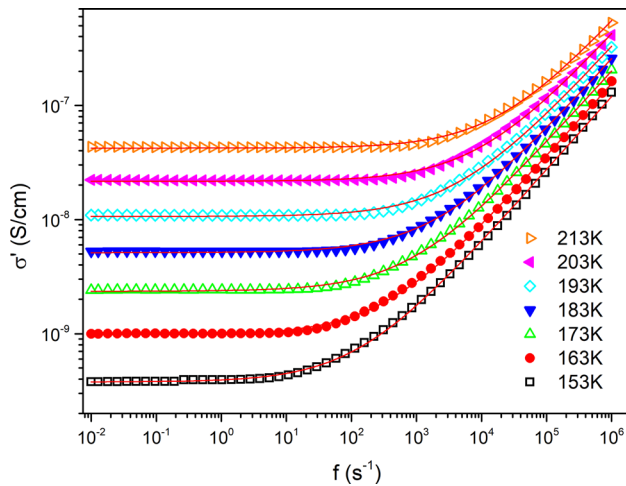


**Figure 10** The frequency dependence of  $\sigma'$  for 50 V/50 T sample with fitted Eq. (2).

theory [16] which takes into consideration the decay of the optical phonons, and therefore a gradual decrease in the activation energy whose temperature dependency can be expressed as:

$$W = W_H \left( \frac{4kT}{hv_o} \right) \tanh \left( \frac{hv_o}{4kT} \right) + W_D, \quad (5)$$

Where  $v_o$  is the optical phonon frequency where  $hv_o/k = \theta_{OP}(el)$ , in which  $\theta_{OP}(el)$  denotes the Debye-like parameter calculated from electrical studies.

Mott proposed that in the temperature region of  $T > \theta_D/2$  and  $T < \theta_D/4$  the conductivity obeys the dependency of [35]:

$$\sigma(T) = \frac{v_{el} e^2 C (1 - C)}{kTR} \exp(-2\alpha R) \exp\left(-\frac{W}{kT}\right), \quad (6)$$

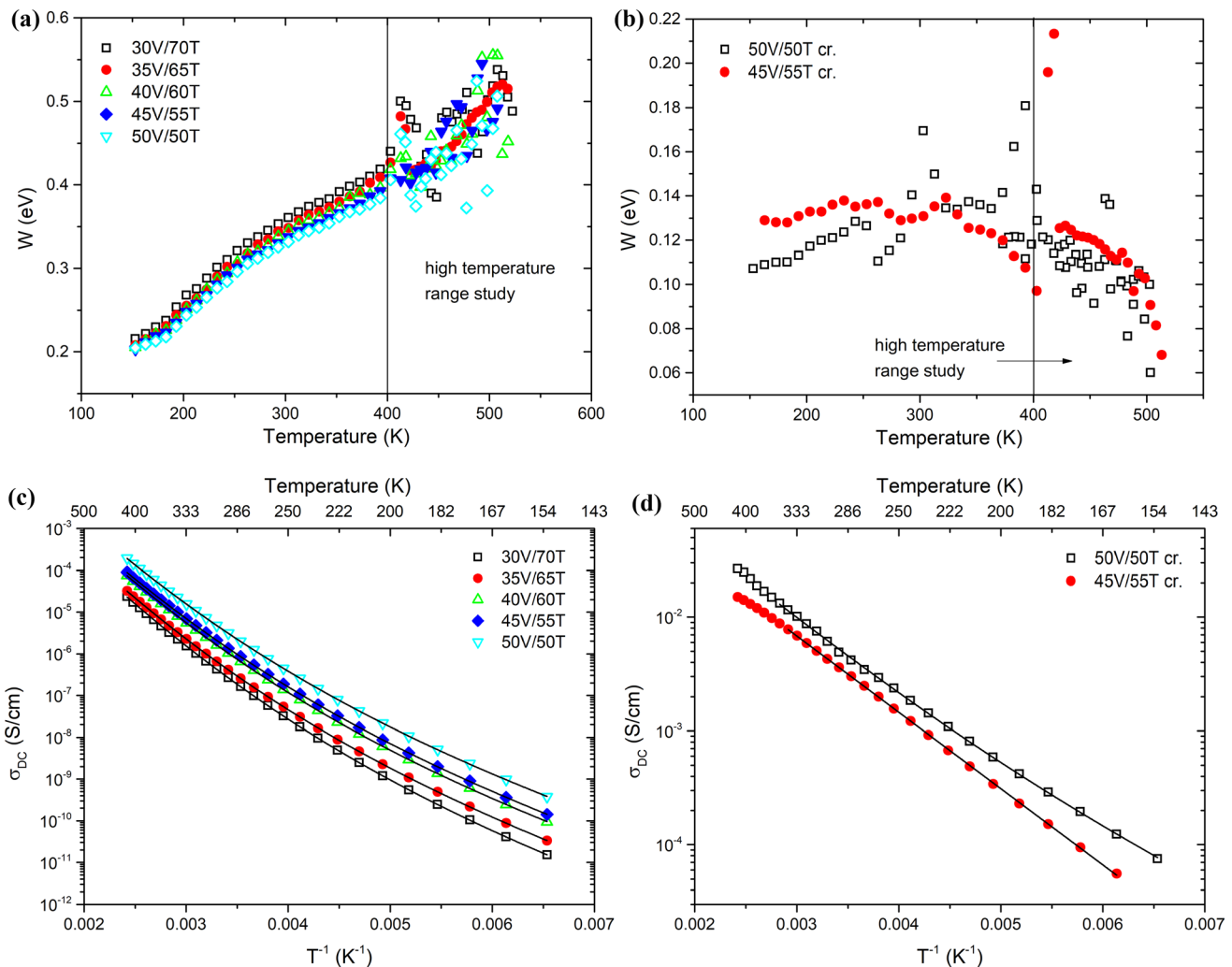


**Figure 11** W plot versus T for **a** glass and **b** glass–ceramics and a plot of conductivity versus  $1/T$  for **c** glass, and **d** glass–ceramics, with fitted Eq. 8, and linear fit (45V/55T cr.).

Where:  $W$  is specified in Eq. (4),  $v_{el}$  is the electron frequency,  $\alpha$  is the rate of wave function decay,  $C$  is the ratio of ion concentration in the low valence state to the total concentration of transition metal ions ( $V^{4+}/(V^{4+} + V^{5+})$ ),  $R$  is the average distance between vanadium ions,  $k$  is the Boltzmann's constant and  $T$  is the absolute temperature. The  $(-2\alpha R)$  factor is related to the fact that electron hopping, in most of the glasses, will not always occur whenever energy levels are aligned, but with the probability of  $p = v_0 \exp(-W/kT)$ .

In Mott's single-phonon approach to SPH, it is stated that activation energy at high temperatures should stabilize to the constant value of  $W = W_H + \frac{1}{2}W_D$ . To determine the temperature ranges appropriate to investigate conductivity dependence in terms of Mott's SPH, one should determine the temperature dependence of activation energy (this would not apply in systems in which another charge carrier is present). One way to do so is to take the derivative of the  $\ln\sigma$  over  $1/T$ :

$$W = -\frac{\partial \ln \sigma(T)}{\partial (\frac{1}{T})}, \tag{7}$$

The temperature dependence plot of  $W$  for glasses and glass-ceramics are shown in Fig. 11a, b. As can be seen in Fig. 11a, activation energy is changing in the whole temperature spectrum of the study, even at temperatures up to  $T_g$ , which is not consistent with the small polaron theory when  $\theta_D = \theta_{AC}$  is considered. Thus, it was concluded that the split of the phonon shares in vanadium-tellurite glasses should be performed using the  $\theta_{OP}$  parameter. However, as the Schnakenberg model is known for its applicability in the whole temperature spectrum, this division of temperature ranges ( $(T > \theta_{OP}/2)$ ,  $(\theta_{OP}/2 > T > \theta_{OP}/4)$ , and  $(T < \theta_{OP}/4)$ ) will only be applied in other models as the separation of multi-phonon and single-phonon dependent ranges.

Figure 11b shows that both crystalline samples exhibit a decrease in activation energy at high temperatures ( $> 350$  K). This behavior was previously seen in crystalline  $V_2O_5$  and was interpreted as free carrier transport resulting from large carrier density [36, 37]. With the decrease in the temperature, activation energy is decreasing only slightly in samples 50V/50T cr., while in sample 45V/55T cr. is stable.

According to the Schnakenberg model, the conductivity of the small polaron hopping in the non-adiabatic regime obeys a temperature dependence of:

$$\sigma(T) = \sigma_0 \exp \left[ -\left( \frac{4W_H}{hv_0} \right) \tanh \left( \frac{hv_0}{4kT} \right) \right] \exp \left( -\frac{W_D}{kT} \right), \tag{8}$$

Where  $\sigma_0$  is equal to:

$$\sigma_0 = \frac{A}{T} \left[ \sinh \left( \frac{hv_0}{kT} \right) \right]^{\frac{1}{2}} \tag{9}$$

Parameters as  $W_H$ ,  $W_D$ ,  $hv_0$  according to the literature [22, 38–41] can be obtained in two ways, one: using Eq. (7), the temperature dependence of the activation energy; and the other from Eqs. (8) and (9). The first method requires two data operations (derivative and fitting) and excludes the  $\sigma_0$  parameter. Therefore, it is concluded that the fitting of Eq. (8) to the conductivity data should give more precise parameters.

In Fig. 11c, d, the temperature dependence of  $\sigma_{DC}$  for glass and glass-ceramic samples is presented. Additionally, the results of Eq. (8) fitting and linear fitting for sample 45V/55T cr. are shown by solid lines. Parameters estimated by fitting are listed in Table 2.

As shown in table 2, the parameter  $W_D$  is constant for almost all of the glass samples and equals  $\sim 0.2$  eV. It should be noted that the values of  $W_D$  depend critically on the applied temperature range as the measuring points at the lowest temperatures correspond to the  $W_D$  value (Fig. 11a, b). It can be seen that the value of  $W_H$  is increasing with a lower vanadium content.  $\theta_{OP}(el)$  is increasing with higher vanadium content. The value of  $\theta_{OP}(el)$  shows a downward trend with a decrease in vanadium content similar to the previously observed decreasing manner of  $\theta_{OP}(IR)$ .

In glass-ceramics, we can observe a significant decrease in the activation energy from  $\sim 0.35$  to  $\sim 0.13$  eV at room temperature (Fig. 11a, b), where the latter is a lower value than the one obtained for crystalline  $V_2O_5$  [36]. In Fig. 11d it can be seen that in sample 50V/50T cr. temperature dependence of conductivity shows curvature characteristic of the SPH. The  $\theta_{OP}(el)$  parameter for the 50V/50T cr. sample is lower than obtained for glass, in agreement with  $\theta_{OP}(IR)$  falling trend.



**Table 2** Parameters of small polaron hopping obtained from Schnakenberg's formula

	A	$W_D(\text{eV})$	$W_H(\text{eV})$	$v_0(10^{13}\text{s}^{-1})$	$\theta_{\text{OP}}(\text{eV})(\text{K})$
Glass					
30V/70T	$4.2 \times 10^4$	0.20	0.42	2.06	983
35V/65T	$5.5 \times 10^4$	0.21	0.41	2.18	1046
40V/60T	$9.1 \times 10^4$	0.20	0.40	2.13	1024
45V/55T	$8.0 \times 10^4$	0.20	0.39	2.15	1030
50V/50T	$1.5 \times 10^5$	0.20	0.39	2.15	1033
Glass–ceramics					
50V/50T cr	$2.7 \times 10^3$	0.11	0.11	1.52	731
45V/55T cr	–	–	–	–	–

In the 45V/55T cr. sample, conductivity shows exponential behavior to around 350 K, the activation energy of which is equal to 0.14 eV, a similar value obtained in crystalline  $\text{VO}_2$  [42]. No change of activation energy with a decrease in temperature, characteristic of SPH, can be noticed. At high temperatures conductivity behavior in the 45V/55T cr. sample changes similarly to the observed in crystalline  $\text{V}_2\text{O}_5$  which most probably is a sign of carrier density increase. Both annealed samples show a temperature dependence of conductivity at the level of crystalline  $\text{VO}_2$  [42]. Schnakenberg model of SPH gives reasonable results for glass and 50V/50T cr. sample.

### Variable range hopping

According to Mott, at low temperatures ( $T < \theta_{\text{OP}}/4$ ) charge transport could occur by VRH. Greaves extended this model to intermediate temperatures. Now we will check both of the VRH models as possible charge transfer mechanisms in our samples. The expression for the conductivity temperature dependence of the VRH model by Mott is based on a single-phonon approach and is given by [15, 43]:

$$\sigma = B \exp(-A/T^{(1/4)}), \quad (10)$$

where  $A$  and  $B$  are constants given by:

$$A = 4[2\alpha^3/9kN(E_F)]^{(1/4)}, \quad (11)$$

$$B = \sigma[e^2/2(8\pi)^{(1/2)}]v_D[N(E_F)/\alpha kT]^{(1/2)},$$

where  $N(E_F)$  is the density of states at the Fermi level.

In Fig. 12 we presented the logarithm of conductivity data for glass (Fig. 12a) and glass–ceramics (Fig. 12b). The data were fitted to Eq. 10 and presented in Fig. 12. Obtained parameters were presented in Table 3.

Now we will apply the VRH by Greaves for the full temperature range. According to Greaves conductivity temperature dependence can be described as [5, 39]:

$$\sigma T^{(1/2)} = C \exp(-D/T^{(1/4)}), \quad (12)$$

Where  $C$  and  $D$  are constants. The slope  $D$  of the fitted function is given by:

$$D = 2.1[\alpha^3/kN(E_F)]^{1/4} \quad (13)$$

In Fig. 13 we presented the logarithm of conductivity data for glass (Fig. 13a) and glass–ceramics (Fig. 13b). The data are fitted to Eq. 13 and presented in Fig. 13. Obtained parameters are presented in Table 3.

As can be seen in Table 3. values of  $N(E_F)$  are similar for both VRH models. Although they are unreasonably large for TMO glass, this model should be checked at lower temperatures.

The models above (Mott SPH, Schnakenberg SPH, and VRH) are assuming a strictly homogenous structure of the conducting material. Phase separation on the molecular level is hard to predict and may be undetectable using standard instruments. Structural studies of the  $\text{V}_2\text{O}_5\text{-TeO}_2$  system indicate that in these glasses vanadium oxide tends to organize in chains of  $\text{V}_2\text{O}_8$  in glass containing more than 30% mol  $\text{V}_2\text{O}_5$  [44]. Therefore, some models, in which phase separation is included, will be examined.

### Friedman-Triberis model

Friedman and Triberis [24] applied the percolation approach in their SPH model and evaluated conductivity and thermopower behavior with temperature changes. In this model, conductive paths can be separated from the less conductive parts of the glass

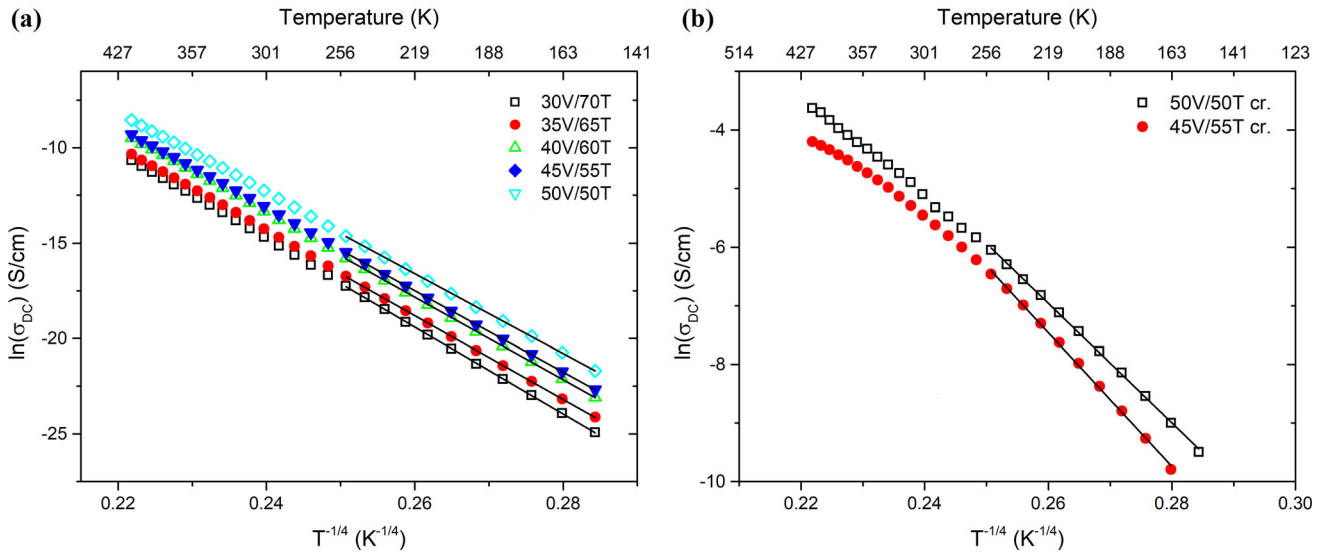


**Figure 12**  $\ln \sigma$  versus  $T^{-1/4}$  of **a** glass and **b** glass–ceramics with a linear fit at  $T < \theta_{OP}/4$ .

**Table 3** The density of states near the Fermi level obtained from VRH models of Mott and Greaves

	$N(E_F)(\text{eV}^{-1} \text{cm}^{-3})$ Mott VRH	$N(E_F)(\text{eV}^{-1} \text{cm}^{-3})$ Greaves VRH
30V/70T	$2.4 \times 10^{28}$	$1.4 \times 10^{28}$
35V/65T	$2.8 \times 10^{28}$	$1.4 \times 10^{28}$
40V/60T	$3 \times 10^{28}$	$1.3 \times 10^{28}$
45V/55T	$3.1 \times 10^{28}$	$1.2 \times 10^{28}$
50V/50T	$3.4 \times 10^{28}$	$1.2 \times 10^{28}$
50V/50T cr	$6 \times 10^{27}$	$4.4 \times 10^{26}$
45V/55T cr	$3.9 \times 10^{27}$	$5.1 \times 10^{26}$

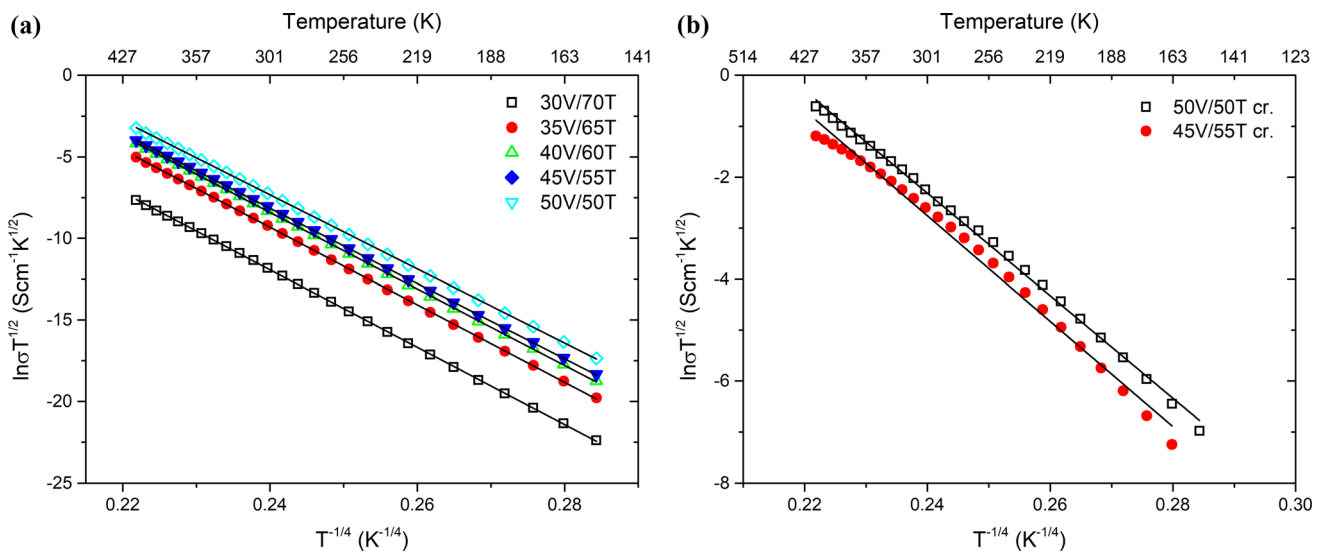


**Figure 13**  $\ln \sigma T^{1/2}$  versus  $T^{-1/4}$  of **a** glass and **b** glass–ceramics with a linear fit at  $T < \theta_D/2$ .

MOST WIEDZY Downloaded from mostwiedzy.pl

in various ways and one should not expect a homogenous distribution of conductive elements in the glass matrix. Considering the effect of correlation between neighboring impedances of better conductive paths in the material they have obtained:

$$\sigma = \sigma_0 \exp(-T_0/T) \sigma^{(1/4)}, \quad (14)$$

where  $\sigma_0$  and  $T_0$  are constants and  $T_0$  is given by

$$T_0 = \begin{cases} \frac{12.5\alpha^3}{kN(E_F)} & \text{for multi-phonon process } T; (\theta_D/2) \\ \frac{17.8\alpha^3}{kN(E_F)} & \text{for single-phonon process } T; (\theta_D/2) \end{cases} \quad (15)$$

Here the density of states near the Fermi level  $N(E_F)$  is assumed constant. As can be seen, this model, similarly to the VRH models, predicts  $T^{-1/4}$  dependence of conductivity. We have applied Eq. 15 to the logarithm of the conductivity data in Fig. 14 as well for the multi-phonon and single-phonon processes. Table 4 presents values of parameters obtained from the slope of the line fitted to the data. For calculations, we assume the value of  $\alpha = 1 \text{ \AA}^{-1}$  [1]. The obtained values of  $N(E_F)$  are consistent with the density of states for oxide glasses. It is clear, that Tribes and Friedman's model provides a good fit for our DC conductivity data.

As can be seen in Table 4 obtained parameters are reasonable for glass and glass-ceramics [45].  $N(E_F)$  is rising for better conductive glass-ceramics. Values of

$N(E_F)$  are similar for the single- and multi-phonon ranges, which confirm the applicability of this model for our materials. In sample 45V/55T, at high temperatures, the fitting is not satisfying.

#### Shimakawa multi-phonon hopping model

To obtain the average distance between vanadium atoms necessary for the Shimakawa multi-phonon hopping model, a density study was performed. Density, molar volume, the concentration of vanadium ions, and the average distance between them were calculated and presented in Table 5. It can be seen that the distance between vanadium ions and density, decreases with increasing vanadium content. Similar results were obtained in previous works [46, 47] as vanadium is replacing tellurium ions in the tellurium glass structure, reducing  $\text{TeO}_4$  units to  $\text{TeO}_3$  units [32].

Shimakawa in his theory presents a model of charge transfer that considers microvoids of air in the glass. In this approach, the distribution of localized states is not homogeneous as in the Mott VRH, Greaves VRH, and Schnakenberg's model of SPH. Because of the porous structure of glass, most of the localized states are located near the dangling bonds on the interface of glass and air in pores. Small separation of the dangling bonds causes the overlapping of the electron's wave function, hence hopping takes place between them. The most resistive, and

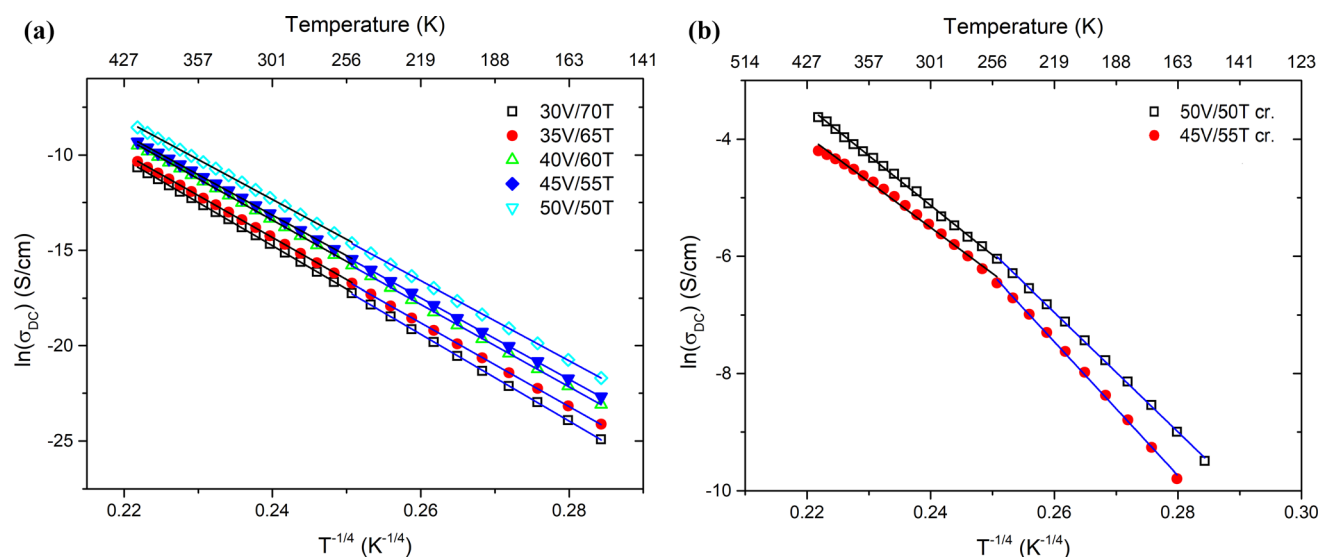


**Figure 14**  $\ln \sigma$  versus  $T^{-1/4}$  of **a** glass and **b** glass-ceramics with a linear fit at temperature ranges of multi-phonon, and single-phonon influence.

**Table 4** Parameters obtained from the Friedman-Triberis model for single-phonon and multi-phonon range

	Single-phonon range		Multi-phonon range	
	$N(E_F)(\text{eV}^{-1} \text{ cm}^{-3})$	$T_0(\text{K})$	$N(E_F)(\text{eV}^{-1} \text{ cm}^{-3})$	$T_0(\text{K})$
30V/70T	$7.6 \times 10^{19}$	$3 \times 10^9$	$5.4 \times 10^{19}$	$2.7 \times 10^9$
35V/65T	$8.9 \times 10^{19}$	$2 \times 10^9$	$6.1 \times 10^{19}$	$2.4 \times 10^9$
40V/60T	$9.4 \times 10^{19}$	$2 \times 10^9$	$6.5 \times 10^{19}$	$2.2 \times 10^9$
45V/55T	$9.9 \times 10^{19}$	$2 \times 10^9$	$7.1 \times 10^{19}$	$2 \times 10^9$
50V/50T	$1.1 \times 10^{19}$	$2 \times 10^9$	$7.5 \times 10^{19}$	$1.9 \times 10^9$
50V/50T cr	$1.9 \times 10^{21}$	$1.1 \times 10^8$	$2.8 \times 10^{21}$	$5.2 \times 10^7$
45V/55T cr	$1.2 \times 10^{21}$	$2 \times 10^8$	$3.8 \times 10^{21}$	$3.8 \times 10^7$

**Table 5** Density  $D$ , molar volume  $V_m$ , the concentration of vanadium ions  $N_{V\text{-ions}}$ , and the average distance between vanadium ions  $R$

Sample IDs	$D \pm 0.01(\text{gcm}^{-3})$	$V_m \pm 0.2 (\text{cm}^3\text{mol}^{-1})$	$N_{V\text{-ions}} \pm 0.01 (\times 10^{21}\text{cm}^{-3})$	$R \pm 0.01(\text{Å})$
30V/70T	4.47	37.2	4.22	6.19
35V/65T	4.27	39.2	4.50	6.06
40V/60T	4.16	40.5	4.79	5.93
45V/55T	3.99	42.6	4.95	5.87
50V/50T	3.90	43.7	4.52	5.78

dominating element in this system would be the hopping of the weakly coupled electron between separated surfaces of the micro clusters [48]. In binary glasses, this model should work similarly as vanadium and tellurium fractions could easily separate and create granules or clusters rich in vanadium, between which multi-phonon hopping could take place. As in the annealed samples, phase separation could occur easily during the crystallization process, we will examine both, glass and glass-ceramics by the Shimakawa approach.

Figure 15 shows  $\log_{10}\sigma_{DC}$  versus  $\log_{10}T$  with a fitted linear function at the temperature  $T > \theta_D/4$  as only multi-phonon influence is considered. As can be seen,  $\sigma_{DC}$  can be proportional to  $T^n$  which is in agreement with the Shimakawa model of conductivity and is well-described by  $\sigma_{DC} = \sigma'_0(T/T_0)^n$  dependency, where  $\sigma'_0$  is a constant depending on the glass composition,  $n$  is a non-integral number, and  $T_0 = hv_0/k$  [6, 39, 48, 49]. Although actual tunneling occurs between micro-clusters separated by the distance  $S$ , hopping distance should be considered in terms of an electron hopping between two centers of granules ( $R$ ) [6, 48, 49]. Delocalized electrons on clusters will couple only to long-wavelength phonons whose frequency is lower than  $v_0 = (a_0/\alpha_e^{-1})v_D$  [50], where  $a_0$  is

the average lattice separation,  $\alpha_e^{-1}$  is effective Bohr radius which is in the order of cluster size  $l_c$ , and  $v_D$  which is the Debye frequency ( $v_D = 2.1 \times 10^{13}\text{s}^{-1}$  for the Debye temperature  $T_D = 1000\text{K}$ ). Assuming cluster size  $l_c = \alpha_e^{-1} = R = 4nm$  and  $a_0$  as V–O–V average distance 0.6 nm (Table 5) parameters  $v_0$  and  $T_0$  equal respectively  $3.6 \times 10^{12}\text{Hz}$  and 150 K.

Mott and Davis [35] proposed general conductivity dependence for hopping given by:

$$\sigma(T) = N_c(eR)^2\Gamma/6kT, \tag{16}$$

where  $N_c$  is the carrier density and it's equal to  $N(E_F)kT$  [6],  $e$  is the electron charge, and  $\Gamma$  is the hopping rate. The hopping rate of the multi-phonon hopping of electrons with weak electron-phonon coupling is described by:

$$\Gamma = [C \exp(-\gamma p)][1 - \exp(-hv_0/kT)]^{(-p)}, \tag{17}$$

where,  $C \approx v_0, p = \Delta/hv_0$ ,  $v_0$  is the acoustic phonon frequency,  $\Delta$  is the difference of localized states' energies, and  $\gamma$  is a measure of electron-phonon coupling. Parameter  $C$  implies the overlapping term  $(-2\chi S)$ , where  $\chi$  is the tunneling parameter [6, 48, 49]. For  $hv_0 < kT$ , Eq. (18) is approximated by [39]:



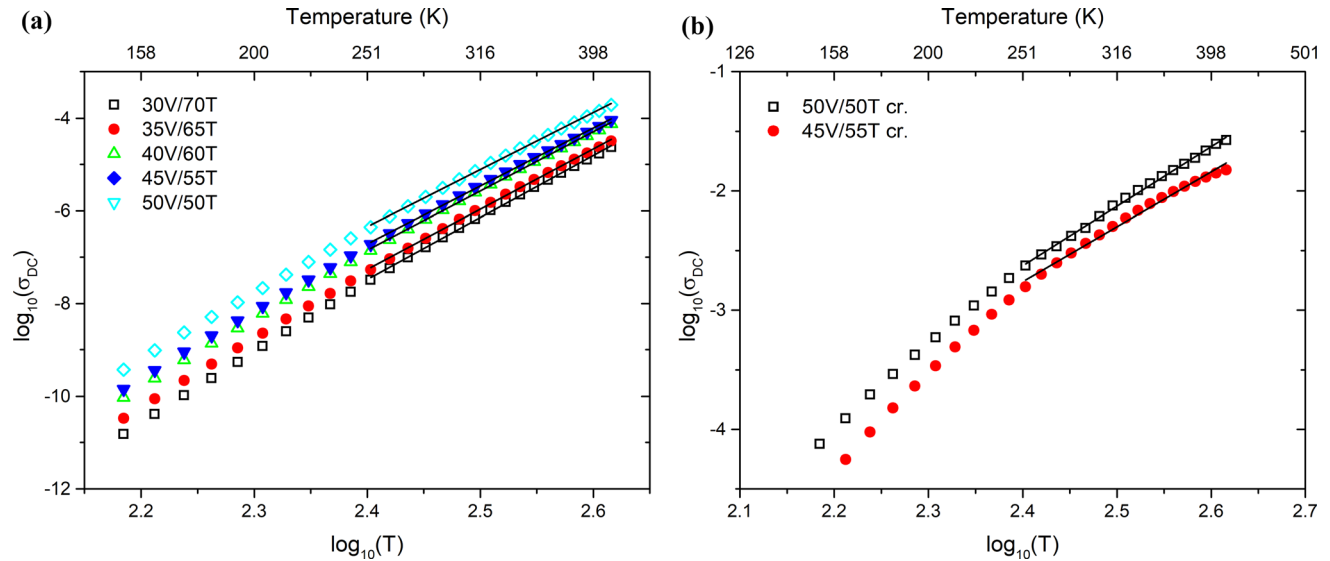


**Figure 15**  $\log_{10}T$  dependency of  $\log_{10}\sigma_{DC}$  of **a** glass, and **b** glass–ceramics with linear fit at the multi-phonon temperature range.

$$\Gamma = [C \exp(-\gamma p)] \left( \frac{T}{T_0} \right)^p \quad (18)$$

It has to be mentioned that parameters  $p$  and  $n$  (since  $p = n$ ) are integral numbers but because of the relation with  $\Delta$  and  $v_0$ , parameters  $p$  and  $n$  are distributed around a certain value which makes them non-integral. Using experimental values  $n$  and combining Eqs. (17) and (19) values  $\gamma$ ,  $\Delta$  and  $\Gamma$  were estimated (assuming  $N(E_F) = 2.9 * 10^{20}$ ) and presented in Table 6.

The conditions of occurring multi-phonon tunneling were presented by Mott and Davis [35], Emin [50], and Englman and Jortner [51]. Mott and Davis showed that  $\gamma$  values should be equal to 2–3. Englman and Jortner showed that the weak coupling transport of an electron should satisfy the condition  $G \leq 1$ , where  $G = (E_M/hv_0)(kT/hv_0)$ . Emin's condition

of a large polaron transport is defined as  $G \ll 1$ . Obtained parameters are presented in tab. 6.

According to Shimakawa [6], hopping rate  $\Gamma$  can be calculated from Fig. 10. We estimated this parameter to be between  $10^1$  and  $10^5 \text{ s}^{-1}$  for glass which is in agreement with values obtained from DC conductivity for glass at low temperatures. A high value of hopping rate for glass–ceramics cannot be compared to AC conductivity as no AC region can be observed, because of their high conductivity. We check the values of parameters  $\gamma$  and  $G$  in the verges of the fitting range. In low temperatures, glass is not fulfilling the conditions of Mott, Davis, and Jortner, although glass–ceramics are fulfilling the conditions in the full range of considered temperatures. As phase separation should occur in the glass–ceramics, Shimakawa multi-phonon hopping should be

**Table 6** Parameters obtained for the Shimakawa multi-phonon hopping model

Sample	$n$	$-\log_{10}\sigma_0$	$\gamma(413\text{K})$	$\gamma(253\text{K})$	$\Delta(\text{eV})$	$G(413\text{K})$	$G(253\text{K})$	$E_M(413\text{K})$	$\Gamma(413\text{K})$	$\Gamma(253\text{K})$
Glass										
30V/70T	13.4	39.6	1.89	1.74	0.17	2.06	1.45	$9.65 \times 10^{-3}$	$2.6 \times 10^7$	$2.2 \times 10^4$
35V/65T	13.0	38.5	1.89	1.74	0.17	1.99	1.99	$9.36 \times 10^{-3}$	$3.6 \times 10^7$	$3.6 \times 10^4$
40V/60T	12.8	37.5	1.84	1.70	0.17	2.07	2.07	$9.70 \times 10^{-3}$	$8.4 \times 10^7$	$9.4 \times 10^4$
45V/55T	12.5	36.8	1.84	1.70	0.16	2.02	2.02	$9.46 \times 10^{-3}$	$1 \times 10^8$	$1.3 \times 10^5$
50V/50T	12.3	36.0	1.79	1.65	0.16	2.09	2.09	$9.80 \times 10^{-3}$	$2.2 \times 10^8$	$3.0 \times 10^5$
Glass–ceramics										
50V/50T cr	5.0	14.6	1.95	2.04	0.06	0.72	0.41	$3.40 \times 10^{-3}$	$3.0 \times 10^{10}$	$1.6 \times 10^9$
45V/55T cr	4.6	13.8	2.12	3.48	0.06	0.56	0.09	$2.61 \times 10^{-3}$	$1.8 \times 10^{10}$	$3.7 \times 10^6$

considered as a possible charge transfer mechanism in the annealed glass.

Schnakenberg model analysis shows that the dependence of  $\theta_{OP}(el)$  agrees well with  $\theta_{OP}(IR)$ . It should be noticed that the optical frequency obtained from the Schnakenberg model fitting ( $\sim 2.15 \cdot 10^{13} \text{ s}^{-1}$ ) is similar to the vibrational frequency of the V–O–V bond in FTIR measurements ( $\sim 2.3 \cdot 10^{13} \text{ s}^{-1}$ ). After crystallization,  $\nu_o$  obtained from Schnakenberg model fitting decreases to  $1.52 \cdot 10^{13} \text{ s}^{-1}$  in 50V/50T cr. which corresponds to the V–O–V band frequency in crystalline  $\text{VO}_2$ .

Friedman-Triberis's model applicability for both glass and glass–ceramics confirm the percolative character of charge transport. Activation energy decrease at high temperatures in annealed samples can be interpreted as a result of a large carrier density which is confirmed by the fitting of the Friedman-Triberis model. The Shimakawa model can be considered in the glass–ceramics as vanadium and tellurium phases should tend to separate, however, SPH seems to be more reasonable considering the crystallization process.

## Conclusions

In  $\text{V}_2\text{O}_5\text{-TeO}_2$  glass with vanadium content higher than 35%mol, crystallization results in a conductivity increase by up to 5 orders of magnitude at room temperature. DSC, XRD, and FTIR studies suggest that the crystallization process leads to the reduction of vanadium ions in the glass matrix that remained after crystallization in the manner shown in Fig. 9, locally increasing the  $\text{V}^{4+}/\text{V}^{5+}$  ratio, which was supported by preliminary XPS studies and recognized as the reason for the conductivity increase. Schnakenberg SPH model fitting showed a decrease of  $W_D$  from 0.20 to 0.11 eV and  $W_H$  from 0.39 to 0.11 eV after crystallization. The decrease in the value of optical phonon frequencies obtained from the Schnakenberg model was in agreement with FTIR studies. Friedman-Triberis percolation model of SPH showed an increase in  $N(E_F)$  from  $10^{19} \text{ eV}^{-1} \text{ cm}^{-3}$  in glasses to  $10^{21} \text{ eV}^{-1} \text{ cm}^{-3}$  in glass–ceramics. Charge transport in both glass and glass–ceramics was recognized as SPH, probably of a percolative nature. Both, the activation energy and conductivity level in samples after crystallization were similar to those previously observed in  $\text{VO}_2$  whose groups increased

presence is supported by FTIR studies. Therefore, it is concluded that the charge transfer in the vanadium-tellurite glass–ceramics occurs by SPH across the percolative channels rich in  $\text{VO}_2$  groups created between the crystalline granules.

## Acknowledgements

Piotr Okoczuk wishes to thank Dr. Tadeusz Miruszewski for valuable discussions about charge transfer in crystalline materials.

## Author contributions

PO–Conceptualization; Data curation; Formal analysis; Investigation; Methodology, Writing-original draft; NAW–Methodology; Writing-review & editing; LM–Investigation; Supervision; Writing-review & editing; LW–Investigation; Supervision; Writing-review & editing; MSŁ–Methodology; analysis; PW–Methodology; Writing-review & editing; BK–Supervision; Writing-review & editing.

## Data availability

The data presented in this study are openly available at: <https://mostwiedzy.pl/pl/piotr-okoczuk,1038332-1/research-data>.

## Declarations

**Conflict of interest** The authors declare that they have no known competing financial interests or personal relationships that could have appeared to influence the work reported in this paper.

**Ethical approval** Not applicable.

**Open Access** This article is licensed under a Creative Commons Attribution 4.0 International License, which permits use, sharing, adaptation, distribution and reproduction in any medium or format, as long as you give appropriate credit to the original author(s) and the source, provide a link to the Creative Commons licence, and indicate if changes were made. The images or other third party material in this article are included in the article's Creative Commons licence, unless indicated

otherwise in a credit line to the material. If material is not included in the article's Creative Commons licence and your intended use is not permitted by statutory regulation or exceeds the permitted use, you will need to obtain permission directly from the copyright holder. To view a copy of this licence, visit <http://creativecommons.org/licenses/by/4.0/>.

## References

- [1] Murawski L, Chung CH, Mackenzie JD (1979) Electrical properties of semiconducting oxide glasses. *J Non Cryst Solids* 32:91–104. [https://doi.org/10.1016/0022-3093\(79\)90066-8](https://doi.org/10.1016/0022-3093(79)90066-8)
- [2] Chung C-H (1979) Electrical properties of semiconducting oxide glasses based on vanadium oxide. University of California
- [3] Flynn BW (1977) Electrical and optical properties of vanadium tellurite glasses. The University of Edinburg
- [4] Mansingh A, Dhawan VK, Sayer M (1983) Dielectric relaxation and modulus of  $V_2O_5$ - $TeO_2$  glasses. *Philos Mag B Phys Condens Matter Stat Mech Electron Opt Magn Prop* 48:215–236. <https://doi.org/10.1080/13642818308228285>
- [5] Greaves GN (1973) Small polaron conduction in  $V_2O_5$ - $P_2O_5$  glasses. *J Non Cryst Solids* 11:427–446. [https://doi.org/10.1016/0022-3093\(73\)90089-6](https://doi.org/10.1016/0022-3093(73)90089-6)
- [6] Shimakawa K (1989) On the mechanism of d.c. and a.c. transport in transition metal oxide glasses. *Philos Mag B Phys Condens Matter Stat Mech Electron Opt Magn Prop* 60:377–389. <https://doi.org/10.1080/13642818908205914>
- [7] Murawski L, Barczyński RJ (1995) Dielectric properties of transition metal oxide glasses. *J Non Cryst Solids* 185:84–93. [https://doi.org/10.1016/0022-3093\(95\)00677-X](https://doi.org/10.1016/0022-3093(95)00677-X)
- [8] Murawski L (1984) AC conductivity in binary  $V_2O_5$ - $P_2O_5$  glasses. *Philos Mag B* 50:L69–L74. <https://doi.org/10.1080/13642818408238888>
- [9] Pietrzak TK, Wasiucionek M, Garbarczyk JE (2021) Towards higher electric conductivity and wider phase stability range via nanostructured glass-ceramics processing. *Nanomaterials*. <https://doi.org/10.3390/nano11051321>
- [10] Garbarczyk JE, Pietrzak TK, Wasiucionek M, Kaleta A, Dorau A, Nowiński JL (2015) High electronic conductivity in nanostructured materials based on lithium-iron-vanadate-phosphate glasses. *Sol State Ion* 272:53–59. <https://doi.org/10.1016/j.ssi.2014.12.019>
- [11] Pietrzak TK, Pawliszak Ł, Michalski PP, Wasiucionek M, Garbarczyk JE (2014) Highly conductive  $90V_2O_5$ - $10P_2O_5$  nanocrystalline cathode materials for lithium-ion batteries. *Proced Eng* 98:28–35. <https://doi.org/10.1016/j.proeng.2014.12.483>
- [12] Pietrzak TK, Michalski PP, Kruk PE, Ślubowska W, Szlachta K, Duda P, Nowiński JL, Wasiucionek M, Garbarczyk JE (2017) Nature of electronic conductivity in olivine-like glasses and nanomaterials of  $Li_2O$ - $FeO$ - $V_2O_5$ - $P_2O_5$  system. *Sol State Ion* 302:45–48. <https://doi.org/10.1016/j.ssi.2016.11.031>
- [13] Pietrzak TK, Wasiucionek M, Nowiński JL, Garbarczyk JE (2013) Isothermal nanocrystallization of vanadate-phosphate glasses. *Sol State Ion* 251:78–82. <https://doi.org/10.1016/j.ssi.2013.01.004>
- [14] Emin D (1982) Small polarons. *Phys Today* 35:34–40. <https://doi.org/10.1063/1.2938044>
- [15] Mott NF (1968) Conduction in glasses containing transition metal ions. *J Non Cryst Sol* 1:1–17. [https://doi.org/10.1016/0022-3093\(68\)90002-1](https://doi.org/10.1016/0022-3093(68)90002-1)
- [16] Schnakenberg J (1968) Polaronic impurity hopping conduction. *Phys Status Sol* 28:623–633. <https://doi.org/10.1002/pssb.19680280220>
- [17] Bridge B, Higazy AA (1986) Acoustic and optical debye temperatures of the vitreous system  $CoO$ - $Co_2O_3$ - $P_2O_5$ . *J Mater Sci* 21:2385–2390. <https://doi.org/10.1007/BF01114282>
- [18] El-Mallawany R (1992) Debye temperature of tellurite glasses. *Phys Status Sol* 130:103–108. <https://doi.org/10.1002/pssa.2211300112>
- [19] El-Mallawany R (1999) Tellurite glasses. Part 2. Anelastic, phase separation, debye temperature and thermal properties. *Mater Chem Phys* 60:103–131. [https://doi.org/10.1016/S0254-0584\(99\)00082-6](https://doi.org/10.1016/S0254-0584(99)00082-6)
- [20] Sidkey MA, El-Mallawany R, Nakhla RIA, El-Moneim A (1997) Ultrasonic attenuation at low temperature of  $TeO_2$ - $V_2O_5$  glasses. *Phys status sol* 159:397–404. [https://doi.org/10.1002/1521-396X\(199702\)159:2%3c397::AID-PSSA397%3e3.0.CO;2-0](https://doi.org/10.1002/1521-396X(199702)159:2%3c397::AID-PSSA397%3e3.0.CO;2-0)
- [21] Szreder NA, Kosiorek P, Karczewski J, Gazda M, Barczy RJ (2014) Microstructure and dielectric properties of barium-vanadate glasses. *Proced Eng* 98:62–70. <https://doi.org/10.1016/j.proeng.2014.12.489>
- [22] Sen S, Ghosh A (1999) Semiconducting properties of magnesium vanadate glasses. *J Appl Phys* 86:2078–2082. <https://doi.org/10.1063/1.371012>
- [23] Dimitriev Y, Dimitrov V, Arnaudov M, Topalov D (1983) IR-spectral study of vanadate vitreous systems. *J Non Cryst Sol* 57:147–156. [https://doi.org/10.1016/0022-3093\(83\)90417-9](https://doi.org/10.1016/0022-3093(83)90417-9)
- [24] Triberis GP, Friedman LR (1985) The effect of the density of states on the conductivity of the small-polaron hopping regime in disordered systems. *J Phys Condens Matter* 18:2281–2286. <https://doi.org/10.1088/0022-3719/18/11/011>

- [25] Degen T, Sadki M, Bron E, König U, Nénert G (2014) The high score suite. *Powder Diffr* 29:S13–S18. <https://doi.org/10.1017/S0885715614000840>
- [26] Wójcik NA, Tagiara NS, Möncke D, Kamitsos EI, Ali S, Ryl J, Barczyński RJ (2022) Mechanism of hopping conduction in Be–Fe–Al–Te–O semiconducting glasses and glass–ceramics. *J Mater Sci* 57:1633–1647. <https://doi.org/10.1007/s10853-021-06834-w>
- [27] Abd El-Moneim A (2002) DTA and IR absorption spectra of vanadium tellurite glasses. *Mater Chem Phys* 73:318–322. [https://doi.org/10.1016/S0254-0584\(01\)00355-8](https://doi.org/10.1016/S0254-0584(01)00355-8)
- [28] Dimitriev J, Arnaudov M, Dimitrov V (1976) IR-Spektralanalyse von glasern des systems  $\text{TeO}_2\text{--V}_2\text{O}_5$ . *Monatshefte für chem* 107:1335–1343. <https://doi.org/10.1007/BF01153912>
- [29] Baia L, Bolboaca M, Kiefer W, Yousef ES, Rüssel C, Breitharth FW, Mayerhöfer TG, Popp J (2004) Spectroscopic studies on the structure of vanadium tellurite glasses. *Phys Chem Glas* 45:178–182
- [30] Ji H, Liu D, Cheng H, Zhang C, Yang L, Ren D (2017) Infrared thermochromic properties of monoclinic  $\text{VO}_2$  nanopowders using a malic acid-assisted hydrothermal method for. *RSC Adv* 7:5189. <https://doi.org/10.1039/c6ra26731a>
- [31] Shafeeq KM, Athira VP, Kishor CHR, Aneesh PM (2020) Structural and optical properties of  $\text{V}_2\text{O}_5$  nanostructures grown by thermal decomposition technique. *Appl Phys A*. <https://doi.org/10.1007/s00339-020-03770-5>
- [32] Sinclair RN, Wright AC, Bachra B, Dimitriev YB, Dimitrov VV, Arnaudov MG (1998) The structure of vitreous  $\text{V}_2\text{O}_5\text{--TeO}_2$ . *J Non Cryst Sol* 232–234:38–43. [https://doi.org/10.1016/S0022-3093\(98\)00544-4](https://doi.org/10.1016/S0022-3093(98)00544-4)
- [33] Jonscher AK (1999) Dielectric relaxation in solids. *J Phys D Appl Phys*. <https://doi.org/10.1088/0022-3727/32/14/201>
- [34] Austin IG, Mott NF (2001) Polarons in crystalline and non-crystalline materials. *Adv Phys* 50:757–812. <https://doi.org/10.1080/00018730110103249>
- [35] Mott NF, Davis EA (1979) Electronic processes in non-crystalline material. (p. 80–113) ISBN 978-0-19-964533-6
- [36] Ioffe VA, Patrino IB (1970) Comparison of the small-polaron theory with the experimental data of current transport in  $\text{V}_2\text{O}_5$ . *Phys Status Sol* 40:389–395. <https://doi.org/10.1002/pssb.19700400140>
- [37] Przeźniak-Welenc M, Szreder NA, Winiarski A, Łapiński M, Kościńska B, Barczyński RJ, Gazda M, Sadowski W (2015) Electrical conductivity and relaxation processes in  $\text{V}_2\text{O}_5$  nanorods prepared by sol-gel method. *Phys Status Sol* 9:2111–2116. <https://doi.org/10.1002/pssb.201552113>
- [38] Murawski L (1993) Electronic cond in oxide glasses. *Pol Ceram Bull* 5:111–122
- [39] Sakata H, Sega K, Chaudhuri BK (1999) Multiphonon tunneling conduction in vanadium-cobalt-tellurite glasses. *Phys Rev B-Condens Matter Mater Phys* 60:3230–3236. <https://doi.org/10.1103/PhysRevB.60.3230>
- [40] Moawad HMM, Jain H, El-Mallawany R (2009) DC conductivity of silver vanadium tellurite glasses. *J Phys Chem Sol* 70:224–233. <https://doi.org/10.1016/j.jpcs.2008.10.009>
- [41] Tashtoush N, Qudah AM, El-Desoky MM (2007) Compositional dependence of the electrical conductivity of calcium vanadate glassy semiconductors. *J Phys Chem Sol* 68:1926–1932. <https://doi.org/10.1016/j.jpcs.2007.05.027>
- [42] Andreev VN, Klimov VA (2007) Electrical conductivity of the semiconducting phase in vanadium dioxide single crystals. *Phys Sol State* 49:2251–2255. <https://doi.org/10.1134/S1063783407120062>
- [43] Mott NF (1969) Conduction in non-crystalline materials III. localized states in a pseudogap and near extremities of conduction and valence bands. *Philos Mag* 19:835–852. <https://doi.org/10.1080/14786436908216338>
- [44] Sakida S, Hayakawa S, Yoko T (2000)  $^{125}\text{Te}$  and  $^{51}\text{V}$  static NMR study of  $\text{V}_2\text{O}_5\text{--TeO}_2$  glasses. *J Phys Condens Matter* 12:2579–2595. <https://doi.org/10.1088/0953-8984/12/12/302>
- [45] Murawski L, Sanchez C, Livage J, Audiere JP (1990) Small polaron transport in amorphous  $\text{V}_2\text{O}_5$  films. *J Non Cryst Sol* 124:71–75. [https://doi.org/10.1016/0022-3093\(90\)91081-2](https://doi.org/10.1016/0022-3093(90)91081-2)
- [46] El-Mallawany R (2003) Glass transformation temperature and stability of tellurite glasses. *J Mater Res* 18:402–406. <https://doi.org/10.1557/JMR.2003.0051>
- [47] Chakraborty S, Boolchand P, Malki M, Micoulaut M (2018) Designing heavy metal oxide glasses with threshold properties from network rigidity. *J Chem Phys*. <https://doi.org/10.1063/1.4855695>
- [48] Shimakawa K (1989) Multiphonon hopping of electrons on defect clusters in amorphous germanium. *Phys Rev B* 39:12933–12936. <https://doi.org/10.1103/PhysRevB.39.12933>
- [49] Shimakawa K, Miyake K (1989) Hopping transport of localized electrons in amorphous carbon films. *Phys Rev B* 39:7578–7584. <https://doi.org/10.1103/PhysRevB.39.7578>
- [50] Emin D (1974) Phonon-assisted jump rate in noncrystalline solids. *Phys Rev Lett* 32:303–307. <https://doi.org/10.1103/PhysRevLett.32.303>
- [51] Englman R, Jortner J (1969) The energy gap law for radiationless transitions in large molecules. *Mol Phys* 18:145–164. <https://doi.org/10.1080/00268977000100171>

**Publisher's Note** Springer Nature remains neutral with regard to jurisdictional claims in published maps and institutional affiliations.



## Terms and Conditions

Springer Nature journal content, brought to you courtesy of Springer Nature Customer Service Center GmbH (“Springer Nature”).

Springer Nature supports a reasonable amount of sharing of research papers by authors, subscribers and authorised users (“Users”), for small-scale personal, non-commercial use provided that all copyright, trade and service marks and other proprietary notices are maintained. By accessing, sharing, receiving or otherwise using the Springer Nature journal content you agree to these terms of use (“Terms”). For these purposes, Springer Nature considers academic use (by researchers and students) to be non-commercial.

These Terms are supplementary and will apply in addition to any applicable website terms and conditions, a relevant site licence or a personal subscription. These Terms will prevail over any conflict or ambiguity with regards to the relevant terms, a site licence or a personal subscription (to the extent of the conflict or ambiguity only). For Creative Commons-licensed articles, the terms of the Creative Commons license used will apply.

We collect and use personal data to provide access to the Springer Nature journal content. We may also use these personal data internally within ResearchGate and Springer Nature and as agreed share it, in an anonymised way, for purposes of tracking, analysis and reporting. We will not otherwise disclose your personal data outside the ResearchGate or the Springer Nature group of companies unless we have your permission as detailed in the Privacy Policy.

While Users may use the Springer Nature journal content for small scale, personal non-commercial use, it is important to note that Users may not:

1. use such content for the purpose of providing other users with access on a regular or large scale basis or as a means to circumvent access control;
2. use such content where to do so would be considered a criminal or statutory offence in any jurisdiction, or gives rise to civil liability, or is otherwise unlawful;
3. falsely or misleadingly imply or suggest endorsement, approval, sponsorship, or association unless explicitly agreed to by Springer Nature in writing;
4. use bots or other automated methods to access the content or redirect messages
5. override any security feature or exclusionary protocol; or
6. share the content in order to create substitute for Springer Nature products or services or a systematic database of Springer Nature journal content.

In line with the restriction against commercial use, Springer Nature does not permit the creation of a product or service that creates revenue, royalties, rent or income from our content or its inclusion as part of a paid for service or for other commercial gain. Springer Nature journal content cannot be used for inter-library loans and librarians may not upload Springer Nature journal content on a large scale into their, or any other, institutional repository.

These terms of use are reviewed regularly and may be amended at any time. Springer Nature is not obligated to publish any information or content on this website and may remove it or features or functionality at our sole discretion, at any time with or without notice. Springer Nature may revoke this licence to you at any time and remove access to any copies of the Springer Nature journal content which have been saved.

To the fullest extent permitted by law, Springer Nature makes no warranties, representations or guarantees to Users, either express or implied with respect to the Springer nature journal content and all parties disclaim and waive any implied warranties or warranties imposed by law, including merchantability or fitness for any particular purpose.

Please note that these rights do not automatically extend to content, data or other material published by Springer Nature that may be licensed from third parties.

If you would like to use or distribute our Springer Nature journal content to a wider audience or on a regular basis or in any other manner not expressly permitted by these Terms, please contact Springer Nature at

[onlineservice@springernature.com](mailto:onlineservice@springernature.com)

